

https://dspace.org/

Study of elastic properties of semiconductors by surface Brillouin scattering

Kotane, Lesias Morake

2010-09-07
http://hdl.handle.net/10539/8622

Downloaded from a DSpace repository. https://dspace.org/

STUDY OF ELASTIC PROPERTIES OF SEMICONDUCTORS BY SURFACE BRILLOUIN SCATTERING

Lesias Morake Kotane

A dissertation submitted to the Faculty of Science, University of the Witwatersrand, Johannesburg, in fulfillment of the requirements for the degree of Master of Science.

Johannesburg, 2010

Declaration

I declare that this dissertation is my own, unaided work. It is being submitted for the Degree of Master of Science in the University of the Witwatersrand, Johannesburg. It has not been submitted before for any degree or examination in any other University.

_____
(Signature of candidate)

_____ day of _____2010

Abstract

Surface Brillouin scattering (SBS) has been used to investigate the elastic properties of two semiconductors.

Boron doped polycrystalline silicon is a widely used material for microelectromechanical systems (MEMS) devices. SBS measurements were carried out on samples of boron doped polycrystalline silicon focusing on the 20ºC to 74ºC temperature range. Rayleigh surface acoustic wave (SAW) and the longitudinal lateral wave velocities were measured allowing the determination of the effective elastic constants C_{11} and C_{44} of the material. The Young's modulus was found to change very little from about 150 GPa in the studied temperature range. On the other hand, the bulk modulus showed a linear decrease from about 124 GPa at 20ºC to about 112 GPa at 74ºC.

Elastic properties of a (100) oriented single crystal of the ternary semiconductor alloy $InAs_{0.91}Sb_{0.09}$ are also reported in this work. This material has become an important focus in the development of optoelectronic devices which operate in the long wavelength transmission window of the atmosphere. SBS was used to measure the angular dependence of the Rayleigh surface acoustic wave (SAW), pseudo surface acoustic wave (PSAW) and the longitudinal lateral wave speeds as a function of direction in the (100) surface to determine the room temperature values of the elastic constants C_{11}, C_{12} and C_{44}. To our knowledge, this is the first time that elastic constants of $InAs_{0.91}Sb_{0.09}$ are reported using the SBS or any other technique.

To my wife Lerato
My daughter Lebogang
And my son Lesedi

Acknowledgements

I would like to thank my supervisors, Professors J.D. Comins and A.G. Every for their guidance, encouragement and support throughout this project. Special mention should be made of Professor Comins' insight, optimism and patience in the laboratory and of Professor Every's exceptional input in all the theoretical and computational work.

I am also grateful to all the staff in the School of Physics Workshop for technical assistance that solved many a problem in the laboratory, to Professor Ludwig Schöning for his expertise in x-ray analysis and to Mr. Rudolph Erasmus for the Raman scattering measurements.

I would also like to thank Dr. B.A. Mathe for his support and advice on numerous measurements and analyses undertaken in this project, Mr. Clemence Sumanya for his patient and tireless work ensuring that the Brillouin scattering apparatus was functioning optimally and Mr. Kudakwashe Jakata for providing a stimulating research environment.

Finally, I wish to thank my wife and the children for their constant support and encouragement throughout this work.

Contents

DECLARATION i

ABSTRACT ii

DEDICATION iii

ACKNOWLEDGEMENTS iv

LIST OF FIGURES vii

LIST OF TABLES x

CHAPTER 1 THEORETICAL BACKGROUND

1.1 Introduction…….. 1

1.1.1 Brillouin scattering, a tool for measuring elastic constants…… 2

1.1.2 Outline of the dissertation……. 4

1.2 Elastodynamics of solids…….. 5

1.2.1 The measurement of elastic constants…… 5

1.2.2 Bulk elastic wave propagation in anisotropic solids.. 6

1.2.3 Bulk elastic wave propagation in isotropic solids.. 7

1.2.4 Surface acoustic wave propagation…… 9

1.3 Surface Brillouin scattering…… 12

1.3.1 Spectral content of SBS spectra…….. 15

1.3.2 SBS cross section and surface elastodynamic Green's function of solids……. 19

1.4 Literature survey……. 21

CHAPTER 2 SBS EXPERIMENTAL METHOD

2.1 Outline……... 22
2.2 The laser…… 25
2.3 The tandem Fabry-Pérot interferometer (TFPI)……. 27
2.4 The detector…….. 29
2.5 The optical furnace…… 31
2.5.1 Temperature control……. 33
2.6 The multichannel analyser……. 34
2.7 Daily setup for SBS measurements…… 34
2.8 Error analysis in SBS measurements……. 38

CHAPTER 3 SBS OF BORON DOPED SILICON

3.1 Introduction……... 40
3.2 Experimental procedure……. 41
3.2.1 Sample preparation…… 41
3.2.2 Sample characterisation……. 42
3.3 Results and discussion…… 44
3.4 Conclusion……. 51

CHAPTER 4 SBS MEASUREMENTS OF $InAs_{0.91}Sb_{0.09}$

4.1 Introduction……. 54
4.2 Sample preparation and characterisation…….. 55
4.3 SBS technique on $InAs_{0.91}Sb_{0.09}$…….. 58
4.3.1 Variation of the Rayleigh SAW…….. 59
4.3.2 Recovery of elastic constants…….. 61
4.4 Conclusion……. 74

CHAPTER 5 CONCLUSION…….. 75
References…… 78
Publications and conference presentations…… 83

List of Figures

1

1.1 The half-space occupying the region $x_3 \leq 0$. The sagittal plane is indicated... 9

1.2 Geometry defined for surface Brillouin scattering. Axis x_3 is pointing outward normal to the surface with light incident in the sagittal x_1x_3 plane. θ_i and θ_s are the incident and scattering angles, respectively, while φ is the azimuthal angle…… 12

1.3 Surface back scattering process [1.12]…… 13

1.4 Calculated Brillouin spectra for various values of the dielectric constant $\varepsilon = \varepsilon_1 + i\varepsilon_2$. (Reproduced from Mills and Subbaswamy [1.14])……. 17

1.5 Measured SBS spectrum for $InAs_{0.91}Sb_{0.09}$ for $k_{||}$ along the [001] direction with the angle of incidence $\theta_i = 71^o$. The Lamb shoulder and the frequencies $\omega_T = v_T k_{||}$ and $\omega_L = v_L k_{||}$ for the transverse and longitudinal thresholds respectively are shown and also the frequency $\omega_R = v_R k_{||}$ for the Rayleigh surface acoustic wave (SAW)…….. 18

2

2.1 Photograph of the SBS apparatus…… 23

2.2 SBS configuration used in this work……... 24

2.3 Etalon loss minimum coinciding laser gain maximum (after Operation manual of Spectra-Physics Model 171 argon ion laser)……... 26

2.4 An aerial view of the JRS instruments (3+3) multipass interferometer, showing A-FP1, B–FP2, C–the detector and D–the shutter.{ FP1, FP2 - Fabry-Pérot} 27

2.5 A plan view of the two Fabry-Pérot interferometers on a single translation stage (after Mock et al. [2.4])……... 28

2.6 Photon detection efficiency for the SPCM-200-PQ detector [2.5]……. 30

2.7 Cross section of the SBS optical furnace…… 32

2.8 Eurotherm 818 temperature controller…… 33

2.9 TFPI in alignment mode, before optimisation (top) and after optimisation (bottom) {from JRS tandem interferometer operation manual}……. 36

3

3.1 Angular dispersion of the Rayleigh surface acoustic wave (SAW) velocity on boron doped silicon……. 43

3.2 A Raman spectrum of boron doped polycrystalline compared to that of crystalline silicon……. 44

3.3 The SBS spectrum for boron doped polycrystalline silicon at 55.6ºC at a scan amplitude of 1.82, mirror spacing of 2.5 mm and the angle of incidence of 70.9º…… 45

3.4 The anti-Stokes component of the SBS spectrum for boron doped polycrystalline silicon at 55.6ºC showing the frequencies $\omega_T = v_T k_{||}$ =19.2 GHz and $\omega_L = v_L k_{||}$ =33.8 GHz for the transverse and longitudinal thresholds respectively and also the frequency $\omega_R = v_R k_{||}$ =16.8 GHz for the Rayleigh surface acoustic wave (SAW). The angle of incidence is fixed at 70.9º……... 46

3.5 Variation of the bulk modulus with temperature for boron doped polycrystalline silicon…….. 50

3.6 Variation of the Young's modulus with temperature for boron doped polycrystalline silicon…….. 51

4

4.1 Laue X-ray photograph of $InAs_{0.91}Sb_{0.09}$ revealing the (100) orientation….. 56

4.2 An example of a standard (100) projection for cubic crystals…… 57

4.3 The variation of the Rayleigh SAW on the (100) surface of the single crystal $InAs_{0.91}Sb_{0.09}$ showing a 90º repeat interval…….. 60

4.4 A typical SBS spectrum of $InAs_{0.91}Sb_{0.09}$ measured at an angle of incidence $\theta_i = 71^o$. The dominant peak arises from the Rayleigh SAW, the longitudinal minimum of the Lamb shoulder can be clearly seen. The shape of the central peak is modified by the shutter that removes the elastically scattered light while introducing a reference signal for the purpose of maintaining the alignment of the interferometer……..... 62

4.5 The measured Stokes component of the SBS spectrum, on an enlarged scale, of $InAs_{0.91}Sb_{0.09}$ for the [001] direction on the (100) surface. The Rayleigh SAW, the transverse threshold $\omega_T = v_T k_{||}$ and the longitudinal threshold $\omega_L = v_L k_{||}$ can be clearly seen. The spectrum was acquired at a scattering angle of 71º……..... 63

4.6 The measured Stokes component of the SBS spectrum, on an enlarged scale, of $InAs_{0.91}Sb_{0.09}$ for the [011] direction on the (100) surface. The Rayleigh SAW, the transverse threshold $\omega_T = v_T k_{||}$ and the longitudinal threshold $\omega_L = v_L k_{||}$ are shown. The spectrum was acquired at a scattering angle of 71º…… 64

4.7 The measured and calculated SBS spectra for the [001] direction on the (100) surface of $InAs_{0.91}Sb_{0.09}$……. 68

4.8 The measured and calculated SBS spectra for the [011] direction on the (100) surface of $InAs_{0.91}Sb_{0.09}$……. 69

4.9 Contour plot of χ^2 in units of $(GPa)^2$ for variation of C_{11} and C_{12} whilst keeping C_{44} fixed at 38.7 GPa……. 71

4.10 Contour plot of χ^2 in units of $(GPa)^2$ for variation of C_{11} and C_{44} whilst keeping C_{12} fixed at 40.4 GPa…… 72

4.11 Contour plot of χ^2 in units of $(GPa)^2$ for variation of C_{44} and C_{12} whilst keeping C_{11} fixed at 73.7 GPa…… 73

List of Tables

1.1 Solutions of Christoffel's equation for cubic symmetry……. 7

3.1 Measured Rayleigh SAW velocities (V_{RSAW}) and Longitudinal velocities (V_L) for selected temperatures……. 47

3.2 Measured elastic constants C_{11}, C_{12} and C_{44} for boron doped polycrystalline silicon…….. 48

3.3 Measured elastic moduli for boron doped polycrystalline silicon for the 20ºC to 73.5ºC temperature range…… 49

4.1 Measured SAW and Longitudinal threshold frequency shifts and their corresponding velocities for the (100) surface of the ternary semiconductor alloy $InAs_{0.91}Sb_{0.09}$……. 65

4.2 Measured and calculated velocities (with a V_L weighting of 0.25) for the (100) surface of the ternary semiconductor alloy $InAs_{0.91}Sb_{0.09}$ …… 67

Chapter 1

Theoretical Background

1.1 Introduction

The science and technology associated with the production of new materials for application in a variety of disciplines has shown an accelerated growth as the demand for better performing materials increases. In this advancement, the processes of designing and manufacturing of materials (with the area of their application in mind), has made it essential to develop and refine ways and means of characterising materials in order to understand their mechanical properties better. For example, the continued and expanding usage of semiconductors as the basic building materials in the construction of a variety of electronic devices requires a better understanding of their performance in different environments. The quest for this better understanding makes the study of elastic properties of materials necessary. This can be made possible by measuring the elastic constants of the materials of interest. Elastic constants provide a means of understanding fundamental interactions that occur in solids, in that they relate mechanical properties of solids to microscopic physical and chemical processes [1.1].

Several methods have been devised for the purpose of measuring elastic constants of materials. Surface Brillouin scattering (SBS) and other methods using ultrasonics, particle and X-ray scattering and neutron scattering are but a few examples of techniques that have been used in studying elastic properties of materials. SBS was the experimental technique utilised in this project.

1.1.1 Brillouin scattering, a tool for measuring elastic constants

Brillouin scattering refers the inelastic scattering of light from thermally induced acoustic waves. Considerable experimental and theoretical progress has been made since the early work of Brillouin (1922) and Mandelshtam (1926). The introduction of a high resolution and high contrast multipass tandem Fabry-Pérot interferometer by Sandercock [1.2], has made measurements of elastic constants of opaque materials possible [1.3]. This paved the way for the now well established experimental technique known as surface Brillouin scattering (SBS).

Surface Brillouin scattering is a contact-free technique that can handle small samples with ease. Measurements can be carried out at both ambient and high temperatures [1.3] and at high pressures as well [1.4]. In SBS studies one mainly measures acoustic excitations localised near the surface of a sample, which may include Rayleigh waves, pseudo-surface acoustic waves, Sezawa and pseudo-Sezawa waves, Love waves, sharp features such as longitudinal lateral waves in the Lamb shoulder and Stoneley interfacial waves.

The measurements are dependent on physical and experimental parameters. The analysis of such excitations makes it possible to determine the elastic constants of thin film materials, superlattices, multilayer systems, elastically soft-on-hard systems [1.5] and elastically hard-on-soft systems [1.6].

In transparent materials light scattering occurs primarily in the bulk of the material. Light is scattered from the phonon-induced fluctuations in the dielectric constant which is referred to as the elasto-optic process. However, in opaque materials light is confined to the near-surface region resulting in a light scattering mainly via a process known as surface ripple scattering. In this process, surface phonons give rise to small amplitude dynamic corrugation of the surface. The surface elastodynamic Green's function methods can then be employed in the treatment of resulting spectral features

of the scattered light. These mechanisms are briefly discussed in this chapter and further details can be found in many references quoted in the literature survey. In both mechanisms the incident light is scattered with a Doppler shift in frequency.

For transparent materials the following situation prevails: A sound wave having a wavevector $\vec{q}$ and angular frequency ω propagating through a medium of dielectric constant ε sets up a modulation in the dielectric constant from which light may be scattered. The scattering interaction obeys the wavevector conservation law

$$\vec{k}_s - \vec{k}_i = \pm \vec{q} \qquad (1.1)$$

where $\vec{k}_s$ and $\vec{k}_i$ are the wavevectors of the scattered light and incident light, respectively and the corresponding frequencies are ω_s and ω_i. The change in the frequency and hence the wavelength of the light is of the order of one part in 10^5 (the ratio of the sound velocity to the velocity of light) and so to a good approximation

$$\left|\vec{k}_s\right| = \left|\vec{k}_i\right| = \frac{2\pi}{\lambda_i} \qquad (1.2)$$

where λ_i is the wavelength of the incident light.

The fluctuations of the dielectric constant can virtually be viewed as a three dimensional phase grating that moves with the velocity of sound v. The resulting Doppler shift (which is the experimentally observed Brillouin frequency shift) can be related to the phonon velocities.

For opaque materials the wavevector conservation is only valid for components parallel to the surface. That is,

$$\vec{k}_{s\|} - \vec{k}_{i\|} = \vec{q}_{\|} \qquad (1.3).$$

The Brillouin frequency shift of the scattered light is equal to the frequency of the phonon causing the scattering, i.e. $\left|\omega_i - \omega_s\right| = \omega$, and hence the surface phonon phase velocity is given by

$$v = \frac{\omega}{q_{\|}} = \frac{|\omega_i - \omega_s|}{q_{\|}} \qquad (1.4).$$

In section 1.3 it is shown how the chosen angle of incidence establishes the modulus of the parallel wavevector and that the measurement of the frequency shift establishes the phonon phase velocity [1.7].

The phonon phase velocity depends on the density and elastic constants of the material. This relation is clearly shown in Table 1.1 where solutions for Christoffel's equation for cubic symmetry are given and in section 1.2.4 where surface wave acoustic wave propagation is discussed. For anisotropic materials, the relationship between the elastic constants and the phase velocities of bulk or surface acoustic waves propagating in different directions in the material can be used to determine the elastic constant tensor which defines the elastic properties of a material.

1.1.2 Outline of the dissertation

A brief theoretical background of SBS together with a synopsis of the elasto-dynamics of solids is given in this chapter. The apparatus and the SBS experimental setup is discussed in Chapter 2. The results of SBS studies on boron doped polycrystalline silicon and the ternary semiconductor alloy $InAs_{0.91}Sb_{0.09}$ are presented in Chapters 3 and 4, respectively. Chapter 5 concludes the dissertation.

1.2 Elastodynamics of solids

From linear elasticity theory, the elastic constant tensor c_{ijkl} relates the elastic stress tensor σ_{ij} to the strain tensor ε_{kl} as follows [1.8]:

$$\sigma_{ij} = c_{ijkl}\varepsilon_{kl} \qquad (1.5).$$

The elastic constant tensor c_{ijkl} is influenced by temperature and pressure, magnetic and electric fields and can vary with frequency, even though it is referred to as a constant. The strain-stress relation can be written as a matrix equation using the Voigt contracted notation. This is achievable as the strain and stress tensors are symmetrical with respect to the interchange of the indices i and j. In the contracted form, the indices range from 1 to 6 corresponding to six independent stress and strain components. That is $c_{ijkl} \rightarrow C_{\alpha\beta}$, $ij \rightarrow \alpha$, $kl \rightarrow \beta$ (i,j,k,l = 1,2,3; α,β =1,…,6). The elements of the stiffness matrix $C_{\alpha\beta}$ are also known as elastic constants. The elastic constant matrix is symmetric across its diagonal i.e. $C_{\alpha\beta} = C_{\beta\alpha}$, so the 6x6 matrix has at most 21 independent components. The number of independent elastic constants is reduced by the existence of materials symmetry. For example, in the case of one of the materials studied in this work which has cubic symmetry, the number of independent elastic constants is reduced to three, namely C_{11}, C_{12} and C_{44}. The other material is isotropic and has only two independent elastic constants, with $C_{12} = C_{11} - 2C_{44}$.

1.2.1 The measurement of elastic constants

The elastic constants, known also as stiffness constants, determine the phase velocities of acoustic waves of different polarisations (quasi-longitudinal and quasi-transverse) propagating in different directions in anisotropic solids and/or of surface

acoustic waves. Measuring the directional dependence of these velocities provides the most important means for determining the elastic constants.

A variety of experimental techniques, such as the Brillouin scattering in the present work, can be employed to measure these phase velocities. The Christoffel equation, referred to in the next section, governs the relation between phase velocities and elastic constants of anisotropic solids. In the high symmetry crystal directions, where the sound waves may be pure transverse modes or pure longitudinal modes, the relationship tends to be simple.

The velocity measurements in these pure mode directions can lead to the determination of an elastic constant that is often a diagonal term of the matrix of elastic constants. For cubic crystals, all elastic constants can be obtained from the bulk wave velocity measurements in such pure mode directions. In crystal symmetries other than the cubic symmetry, velocity measurements in non-pure mode directions sometimes need to be utilised to determine the remainder of the non-diagonal terms of the elastic constant matrix.

1.2.2 Bulk elastic wave propagation in anisotropic solids

The Christoffel equation

$$\left(\Gamma_{jk} - \rho v^2 \delta_{jk}\right) U_k = 0 \;\; ; j = 1,2,3 \qquad (1.6)$$

governs the behaviour of elastic waves propagating in an elastic, homogeneous anisotropic solid. In this equation we have $\Gamma_{jk} = l_i l_l c_{ijkl}$ which is called the Christoffel matrix having elements dependent on the wave propagation direction, specified by l_i, the direction cosines of the wavevector, and the stiffness constants c_{ijkl} of the solid. The density of the material is ρ, U_k are the displacements in the respective Cartesian axes and δ_{jk} is the Kronecker delta. The phase velocity is v. The determinant of the

coefficients is equated to zero in order to find the non-trivial solution for the displacements. The following cubic secular equation for ρv^2 is obtained

$$\left|\Gamma_{jk} - \rho v^2 \delta_{jk}\right| = 0 \qquad (1.7).$$

The roots of this equation correspond to longitudinal (L), slow transverse (ST) and fast transverse (FT) modes. Hence, given the directions along which the phase velocity measurements are taken, equations for the elastic constants can be obtained. For the propagation along symmetry directions, the cubic equation factorises and simple linear or quadratic equations are obtained for the respective velocities. The solutions are listed in Table 1.1 for the case of a medium of cubic symmetry.

Table 1.1: Solutions of Christoffel's equation for cubic symmetry (reproduced from Every [1.9]).

Propagation direction **n**	Polarization direction **U**	Wave mode	Velocity equation $\rho v^2 =$	
[100]	[100]	L	C_{11}	(a)
[100]	[010], [001]	$T(2)$	C_{44}	(b)
[110]	[001]	T	C_{44}	(c)
[110]	$[1\bar{1}0]$	T	$\frac{1}{2}(C_{11} - C_{12})$	(d)
[110]	[110]	L	$\frac{1}{2}(C_{11} + C_{12} + 2C_{44})$	(e)
[111]	$[1\bar{1}0]$, $[11\bar{2}]$	$T(2)$	$\frac{1}{3}(C_{11} - C_{12} + C_{44})$	(f)
[111]	[111]	L	$\frac{1}{3}(C_{11} + 2C_{12} + 4C_{44})$	(g)
$[\cos\theta, \sin\theta, 0]$	[001]	T	C_{44}	(h)
$(\cos\theta, \sin\theta, 0)$	(001) plane	qL, qT	$\frac{1}{2}\left\{B \pm \sqrt{B^2 - 4C}\right\}$	(i)

1.2.3 Bulk elastic wave propagation in isotropic solids

Isotropic solids are materials that exhibit elastic behaviour that is independent of the direction of propagation of the elastic wave. Examples of isotropic solids are ceramics, polycrystalline materials with no preferred orientation and amorphous

materials. Isotropic materials can be adequately characterised by two independent elastic constants c_{11} and c_{44}, with $c_{12} = c_{11} - 2c_{44}$.

Often however, Lamé constants λ and μ are used to describe elastic properties of isotropic solids. The correspondence between these different constants is

$$c_{12} = \lambda \ , \ c_{44} = \mu \qquad \text{and } c_{11} = \lambda + 2\mu \tag{1.8}$$

For engineering purposes, elastic properties of isotropic materials are quoted in terms of the Young's modulus E, the shear modulus G, the bulk modulus K and the Poisson's ratio v.

Young's modulus E, is defined as the tensile (normal) stress divided by the longitudinal strain for a rod, and it is readily established that

$$E = \frac{\mu(3\lambda + 2\mu)}{(\lambda + \mu)} \ = \frac{c_{44}(3c_{12} + 2c_{44})}{(c_{12} + c_{44})} \tag{1.9}$$

Poisson's v, is the negative of the ratio of the transverse strain to the longitudinal strain for a rod and is given by

$$v = \frac{\lambda}{2(\lambda + \mu)} = \frac{c_{12}}{2(c_{12} + c_{44})} \tag{1.10}$$

Shear modulus G**,** is the applied shear stress divided by the resulting shear strain, hence

$$G = \mu = c_{44} \tag{1.11}$$

Bulk modulus K, is the negative of the ratio of pressure to the relative change in volume and

$$K = \frac{(3\lambda + 2\mu)}{3} = \frac{(3c_{12} + 2c_{44})}{3} \tag{1.12}$$

The four engineering constants mentioned above are related in various ways such as:

$$K = \frac{E}{3(1-2v)} \tag{1.13}$$

and $$v = \frac{E}{2G} - 1 \qquad (1.14).$$

1.2.4 Surface acoustic wave propagation

In this section a brief outline of the propagation of surface acoustic waves is given with the ultimate aim of establishing a relationship between the surface acoustic wave (SAW) velocity and the material's elastic constants with a special focus on high symmetry directions. The Rayleigh SAW is a superposition of three phase-matched evanescent waves that satisfies the free surface boundary conditions such that the amplitude of the Rayleigh SAW falls off to a negligible value within a few wavelengths of the surface.

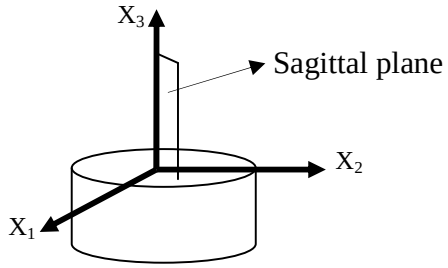


Figure 1.1: The half-space occupying the region $x_3 \leq 0$. The sagittal plane is indicated.

We make use of figure 1.1 to consider the form of the boundary conditions. The orientation of the coordinate system gives the x_1 and x_2 axes in the plane surface of a material and the x_3 axis is normal to it. The boundary conditions are that the traction forces (forces exerted by the solid across the surface) should be zero since there is nothing on the other side of the surface to react against. These boundary conditions thus take the form

$$\sigma_{3j} = 0 \text{ at } x_3 = 0 \qquad \text{for } j = 1,2,3 \qquad (1.15).$$

Through the stress-strain relationship the traction forces can be expressed in terms of the displacement field, yielding 3 equations for the 3 partial wave amplitudes. The corresponding secular equation in turn yields the Rayleigh SAW velocity. While

straightforward to solve numerically, this is a cumbersome problem to solve analytically in the general case. The problem can be simplified when a material's symmetry is taken into consideration. For situations where the sagittal plane is a material's symmetry plane, the problem is reduced to having two sagittally polarised modes that must satisfy only two boundary conditions. These are decoupled from the horizontally polarised (SH) shear mode.

The details of this discussion are presented by Royer and Dieulesaint [1.10] where an algebraic technique is employed in obtaining the following implicit equation for the Rayleigh SAW velocity propagating on the surface of a crystal with a hexagonal symmetry

$$\rho V_{RSAW}^2 - \left(\frac{C_{22}}{C_{66}} \times \frac{C_{66} - \rho V_{RSAW}^2}{C_{11} - \rho V_{RSAW}^2} \right)^{\frac{1}{2}} \times \left(C_{11} - \frac{C_{12}^2}{C_{22}} - \rho V_{RSAW}^2 \right) = 0 \qquad (1.16)$$

where V_{RSAW} is the Rayleigh surface acoustic wave (Rayleigh SAW) velocity and ρ is the density of the material. The above equation can be reformulated for cubic symmetry where the Rayleigh SAW propagates along the [100] direction in the (001) plane by making the replacements $C_{66} \to C_{44}$ and $C_{22} \to C_{11}$. Hence

$$\rho V_{RSAW}^2 - \left(\frac{C_{11}}{C_{44}} \times \frac{C_{44} - \rho V_{RSAW}^2}{C_{11} - \rho V_{RSAW}^2} \right)^{\frac{1}{2}} \times \left(C_{11} - \frac{C_{12}^2}{C_{11}} - \rho V_{RSAW}^2 \right) = 0 \qquad (1.17).$$

This equation is used in Chapter 4 where a crystalline material with a cubic symmetry is discussed.

In moving from the [100] direction in the (001) cube plane to the [110] direction, the Rayleigh SAW becomes more deeply penetrating, its intensity decreases in SBS and it ultimately degenerates with the limiting transverse bulk wave. A surface-like wave which slowly radiates energy away from the surface and for which the displacement field does not vanish at infinite depth, emerges from the bulk wave continuum. This wave has its energy mainly confined near the surface and it is known as a pseudo-

surface acoustic wave (PSAW) [1.11]. In the [110] direction it becomes a true non-radiating supersonic SAW.

In a manner similar to the Rayleigh SAW velocity, an algebraic equation for the PSAW velocity propagating in the [110] direction of a crystalline material with a cubic symmetry is given by equation (1.18).

$$\rho V_{PSAW}^2 - \left(\frac{C_{11}}{C_{44}} \times \frac{C_{44} - \rho V_{PSAW}^2}{\left\{ \frac{1}{2}\left(C_{11} + C_{12} + 2C_{44}\right) \right\} - \rho V_{PSAW}^2} \right)^{\frac{1}{2}} \times \left(\frac{1}{2}\left(C_{11} + C_{12} + 2C_{44}\right) - \frac{C_{12}^2}{C_{11}} - \rho V_{PSAW}^2 \right) = 0 \qquad (1.18)$$

with V_{PSAW} being the pseudo surface acoustic wave velocity.

The way in which we use equations (1.16) and (1.18) for the SAW and PSAW for determining elastic constants for cubic symmetry is novel and will be expounded on further in Chapter 4.

For isotropic symmetry $C_{12} = C_{11} - 2C_{44}$ and equation (1.17) takes on the form

$$\rho V_{RSAW}^2 - \left(\frac{C_{11}}{C_{44}} \times \frac{C_{44} - \rho V_{RSAW}^2}{C_{11} - \rho V_{RSAW}^2} \right)^{\frac{1}{2}} \times \left(C_{11} - \frac{\left(C_{11} - 2C_{44}\right)^2}{C_{11}} - \rho V_{RSAW}^2 \right) = 0 \qquad (1.19).$$

This equation, which depends only on two independent elastic constants, is used in Chapter 3 in determining the elastic constants of boron doped silicon.

1.3 Surface Brillouin scattering

With this study being on the utilisation of the surface Brillouin scattering technique in the characterisation of elastic properties of semiconductors, it is important that a discussion is led on basic aspects of scattering from surfaces. Surface Brillouin scattering involves light scattering at or near the surface of materials. This is largely the case for materials with a high optical absorption where the penetration depth of the incident light is restricted to a volume close to the surface. As stated in section 1.1, the incident light is scattered from the dynamic corrugation on the surface of the sample mainly via the surface ripple mechanism as illustrated in figure 1.3. Consider the geometry for surface Brillouin scattering shown below in figure 1.2. The nomenclature is discussed in section 1.1.1.

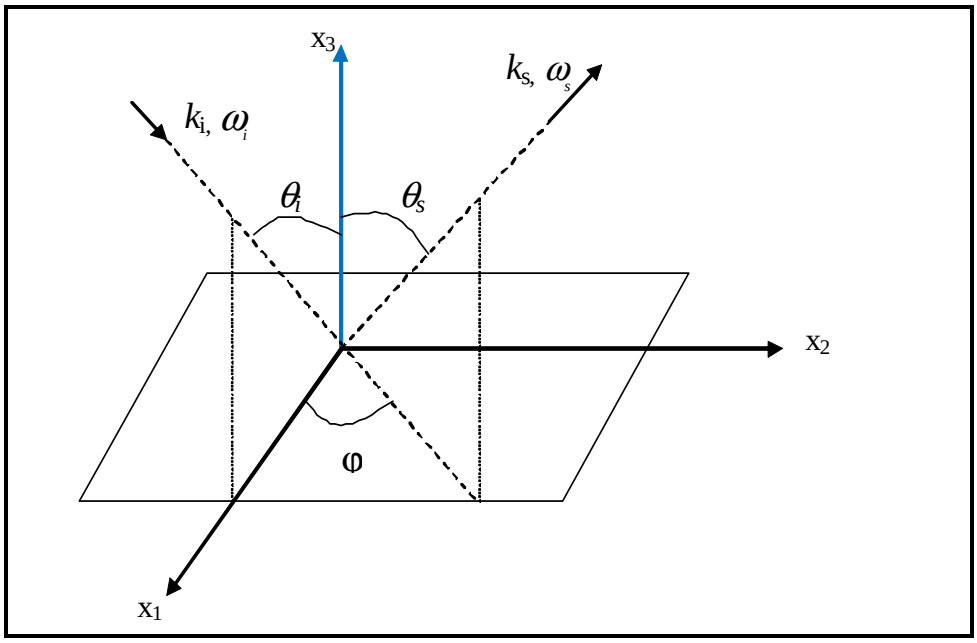


Figure 1.2: Geometry defined for surface Brillouin scattering. Axis x_3 is pointing outward normal to the surface with light incident in the sagittal x_1x_3 plane. θ_i and θ_s are the incident and scattering angles, respectively, while φ is the azimuthal angle.

Figure 1.3 shows a 180º backscattering geometry where $\theta_i = \theta_s$ and $\varphi = 0$.

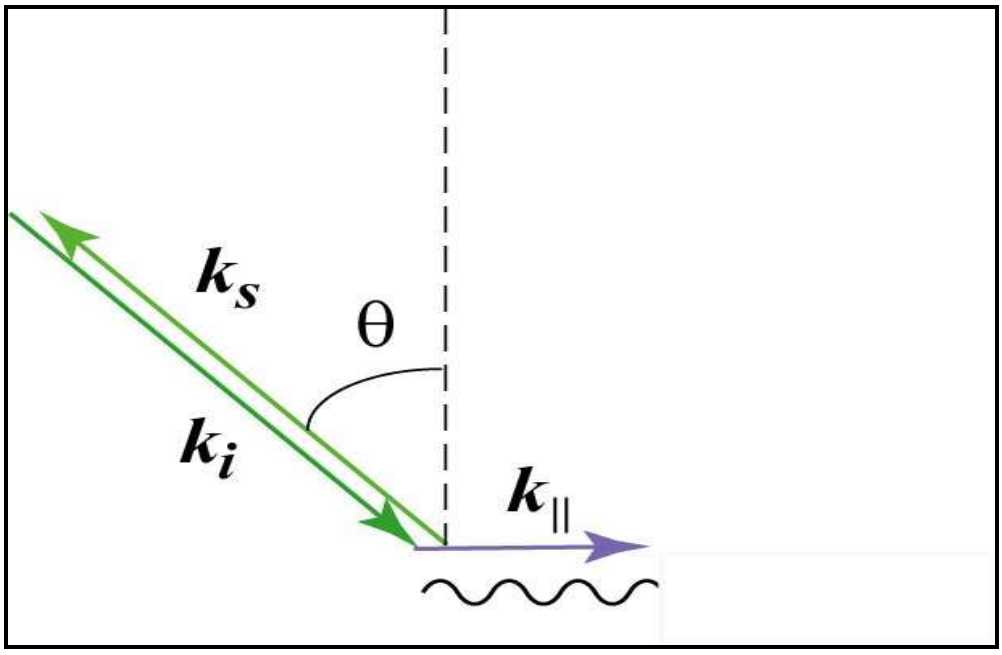


Figure 1.3: 180º back scattering geometry where $\theta_i = \theta_s = \theta$ [1.12].

In these materials with high optical absorption i.e. opaque materials, the coupling of the light is due mainly to surface acoustic waves (SAW's) which have displacements essentially localised in an area close to the surface. The following brief discussion highlights the two equations that provide a description of the conditions for light scattering by surface acoustic waves.

We have already seen that when scattering occurs near the surface, the conservation of momentum only applies to the components parallel to the surface. It then follows from figure 1.3 that the conservation of momentum for SAW's in a backscattering geometry leads to

$$k_{||} = 2k_i \sin\theta_i \qquad (1.20)$$

where θ_i is the incident angle of the laser light. The relationship between the surface phonon velocity and the frequency shifts can be shown by a consideration of the conservation of energy.

Thus,

$$\omega_s - \omega_i = 2k_i \sin\theta_i \, v \tag{1.21}$$

with $(\omega_s - \omega_i)$ being the frequency shift and v the surface phonon phase velocity. The scattering of light at the surface of a material can also be caused by bulk waves incident on the surface. When scattering by a bulk wave having wavevector K_b in the sagittal plane (defined by the normal to the surface and the phonon propagation direction) is considered, from conservation of momentum components parallel to the surface, we have

$$K_{b\|} = 2k_i \sin\theta_i = K_b \cos\phi \tag{1.22}$$

where ϕ is the angle between the wavevector K_b and the sample surface. In this case the frequency shifts $(\omega_s - \omega_i)$ are related to the bulk wave velocity by the equation

$$\omega_s - \omega_i = \frac{2k_i \sin\theta_i \, v}{\cos\phi} \tag{1.23}.$$

It can be noted that the equations contain ϕ, which means that the spectrum is a continuum starting at a threshold defined by setting $\phi = 0$, and v equal to the slowest transverse velocity v_T

$$(\omega_s - \omega_i)_{\min} = 2k_i \sin\theta_i \, v_T \tag{1.24}$$

and extending to higher frequencies. The surface scattering of light by the bulk wave with a wavevector parallel to the surface of the material, is represented by this threshold. As we will see later there is also a threshold within the continuum corresponding to the bulk longitudinal velocity v_L, and possibly one or more other threshold.

The preceding discussion demonstrates that both the SAW's and the bulk waves can scatter incident light at the surface of a material. The opacity of the material tends to determine the effectiveness of the ripple scattering and/or the elasto-optic mechanism in producing the Brillouin spectrum; a detailed discussion on this topic appears in Nizzoli and Sandercock [1.13]. For example, in semi-opaque materials, such as semiconductors which are the subject of this study, the two mechanisms contribute to observed SBS spectral features even though the ripple mechanism dominates over the elasto-optic mechanism [1.1].

1.3.1 Spectral content of SBS spectra

The role of the penetration depth of the incident light is illustrated in figure 1.4 which shows the calculated Brillouin spectra for various values of the dielectric constant $\varepsilon = \varepsilon_1 + i\varepsilon_2$ calculated by Mills and Subbaswamy [1.14]. The real part ε_1 has been fixed at a value of 10.0 while the imaginary ε_2 is varied from values of 0.01 (transparent materials) to 10.0 (highly opaque materials). For $\varepsilon_2 = 0.01$, a large volume is illuminated and the scattering occurs mainly via the elasto-optic mechanism resulting in the transverse acoustic (TA) and longitudinal acoustic (LA) Brillouin peaks which are narrow and intense. However, with an increase in ε_2, meaning an increase in absorption, their intensities decrease (note the change in scale) and the peaks broaden.

For $\varepsilon_2 = 1.0$, there is a growing importance of the ripple scattering mechanism such that low-frequency excitations, including the Rayleigh surface acoustic wave (R), become dominant. A broad continuum associated with the ripple scattering of the bulk waves is clearly visible.

Finally, for highly opaque materials, $\varepsilon_2 = 10.0$, light scattering by elasto-optic coupling is negligible. The Rayleigh surface acoustic wave peak and the continuum from bulk wave scattering via the surface ripple mechanism are dominant. This continuum is known as the Lamb shoulder. The Lamb shoulder arises from a combination of transverse and longitudinal modes.

The SBS spectrum, such as the one dominated by the ripple mechanism, can be calculated by the surface elastodynamic Green's function and hence the spectral features can be readily analysed. Typically, a surface ripple scattering dominated spectrum (see figure 1.5 as an example) displays a sharp peak at the low frequency end associated with the Rayleigh SAW or PSAW and a less intense Lamb shoulder extending from the transverse threshold, $\omega_T = v_T k_{||}$, to higher frequencies. In the region $\omega_T < \omega < \omega_L$ of the Lamb shoulder, the longitudinal modes are evanescent whereas the transverse modes are homogeneous and beyond the longitudinal threshold, $\omega_L < \omega$, both the longitudinal modes and the transverse modes are homogeneous.

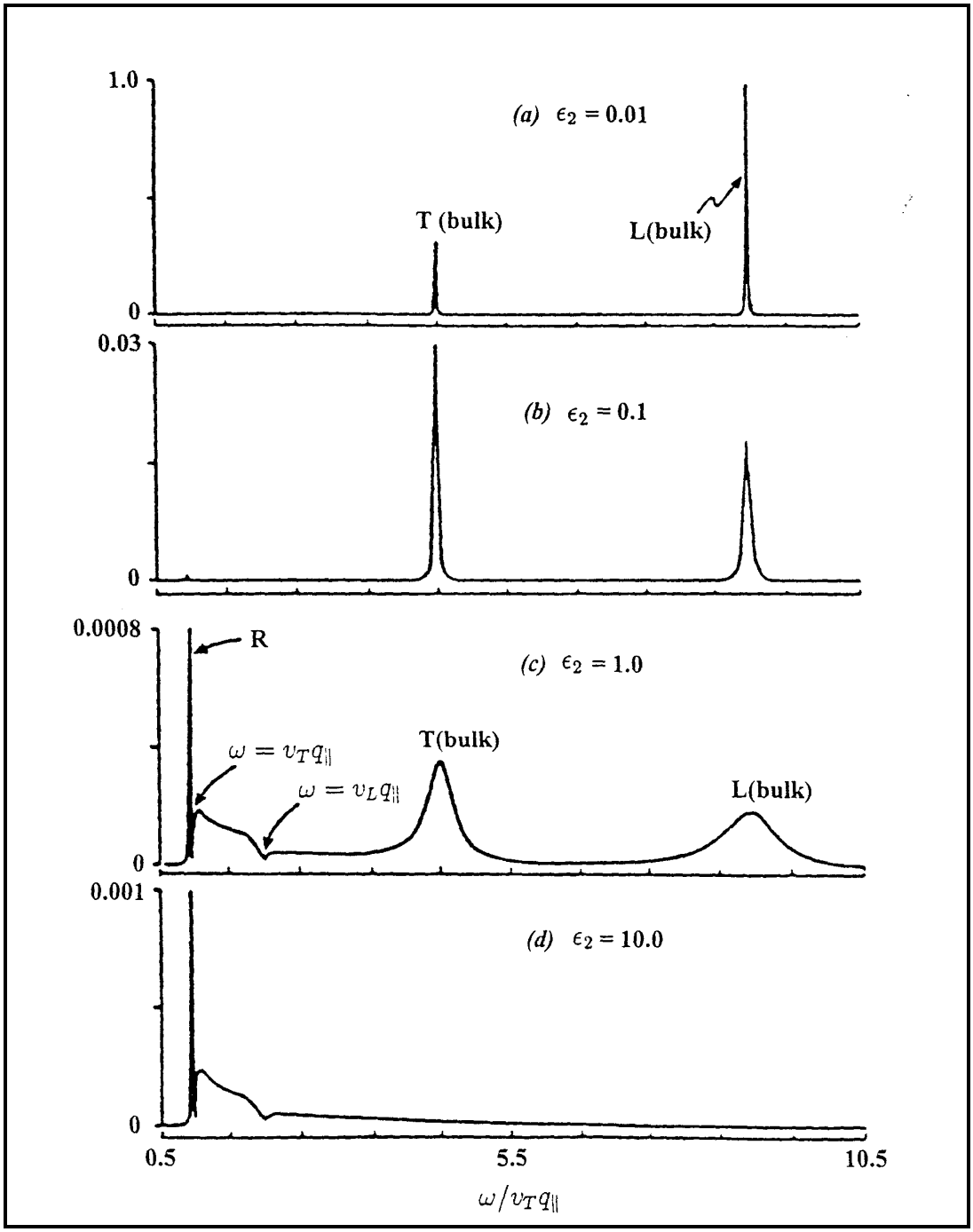


Figure 1.4: Calculated Brillouin spectra for various values of the dielectric constant $\varepsilon = \varepsilon_1 + i\varepsilon_2$. (Reproduced from Mills and Subbaswamy [1.14]).

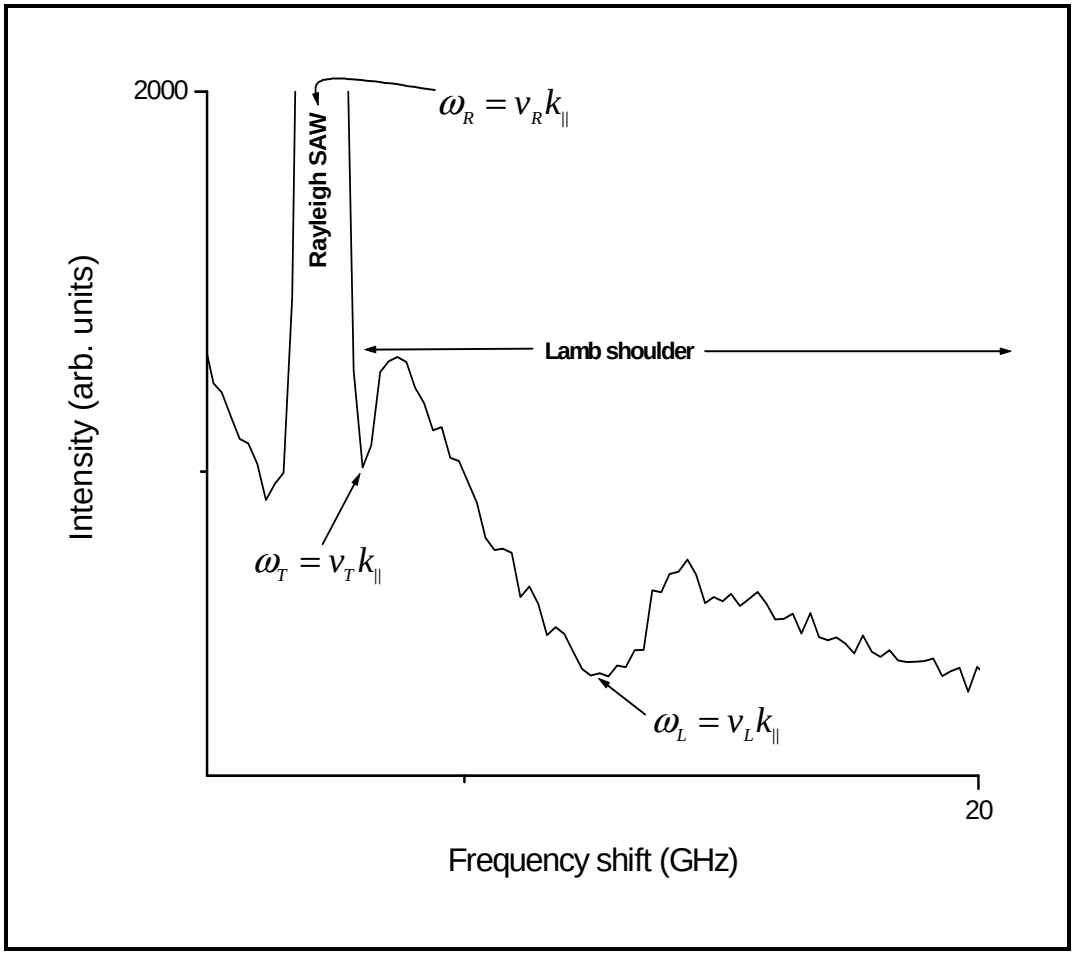


Figure 1.5: Measured SBS spectrum for $InAs_{0.91}Sb_{0.09}$ for $k_{||}$ along the [001] direction with the angle of incidence $\theta_i = 71°$. The Lamb shoulder and the frequencies $\omega_T = v_T k_{||}$ and $\omega_L = v_L k_{||}$ for the transverse and longitudinal thresholds respectively are shown and also the frequency $\omega_R = v_R k_{||}$ for the Rayleigh surface acoustic wave (SAW).

1.3.2 SBS cross section and surface elastodynamic Green's function of solids

References [1.15 – 1.20] provide a detailed discussion on the SBS cross section and can be consulted for further reading on this subject. It should be pointed out at this stage that the discussion on the SBS cross section that follows does not include the angular dependence (*variation of the cross section with the incidence angle of the p-p reflection coefficient*) of the Brillouin scattering cross section as discussed by Loudon and Sandercock [1.21]. The symbol *p* refers to the polarization in the sagittal plane. Their discussion, in part, sought to explain the discrepancy between acoustic velocities determined using SBS and those obtained from ultrasonic measurements. Furthermore, the computational approach developed by Every et al. [1.19] and Zhang et al. [1.20] for solving the free surface Green's function problem has proved to be a less cumbersome method that has been found to be very successful in the interpretation of SBS spectra.

Hopefully, the brief discussion that follows will not do any injustice to detailed discussions referred to above.

The scattering of light from the surface of a half space, that is $x_3 \leq 0$ as in figure 1.1, is considered. As we have seen, for nearly opaque materials, the surface ripple mechanism of light scattering dominates the elasto-optic coupling and can provide a good description of light scattering by surface acoustic phonons.

The scattering cross section for ripple scattering by a surface acoustic excitation of angular frequency ω and surface-wave wavevector $k_{\|}$, is proportional to the power spectrum of the thermally excited normal displacements of the surface at that frequency and with that wavevector. Additionally, for sufficiently high temperatures

(e.g. room temperature) $T \gg \hbar\omega / k_B$ where k_B is Boltzmann's constant, the SBS efficiency or cross section takes the form

$$I(\omega) = D\frac{T}{\omega}\mathrm{Im}\left\{G_{33}\left(k_{\|},\omega\right)\right\} \tag{1.25}$$

where D is a constant that depends on the optical properties of the medium, the scattering geometry and the frequency and polarisation of the incident light. G_{33} is the component of the Fourier domain elasto-dynamic Green's function and for the half space it is given by

$$G_{33}\left(k_{\|},\omega\right) = \sum_{n=1}^{3}\frac{i}{\omega}\frac{adj\left(B\right)_3^{(n)}}{\left|B\right|}U_3^{(n)} \tag{1.26}$$

in which

$$B_l^{(n)} = \sum_{pq} C_{3lpq}U_p^{(n)}k_q^{(n)} / \omega \tag{1.27}.$$

The boundary condition matrix is given by B and $U_3^{(n)}$ are the x_3 components of the polarization vectors. In surface Brillouin scattering, $k_{\|}$ is determined by the experimental arrangement and the scattering geometry and the Brillouin intensity $I(\omega)$ is a function of the angular frequency shift in the measured spectrum. When half space materials are considered, the Brillouin-scattering spectrum consists of one sharp line associated with the true Rayleigh SAW and then at higher frequencies a continuum of excitations extending from a threshold, known as the transonic state, to higher frequencies. A true surface wave (SAW) arises when B^{-1} becomes singular. The nature of excitations depends on the real and complex values of the wavevectors, $k_3^{(n)}$, of the partial waves. There are resonances which can be observed within the frequency region of the Lamb shoulder; these are associated with pseudo surface acoustic waves (PSAW). In this study we used a FORTRAN based computer program developed over the years with the principal assistance of Professor A.G. Every, for the calculation of the Rayleigh SAW's, pseudo SAW's and the Lamb shoulder, particularly the longitudinal threshold, in the analysis of SBS spectra.

1.4 Literature survey

The general principles of Brillouin scattering, particularly surface Brillouin scattering, that are relevant to the measurements reported in later chapters were the ones of particular interest. Detailed theoretical descriptions of the elastic properties of solids have been presented in numerous texts such as the one by Every [1.9] and the references therein. The theory of light scattering from corrugated surfaces was developed by amongst others Maradudin and Mills [1.22], Agarwal [1.23] and Marvin et al. [1.24]. The understanding of the SBS theory was further aided by the development of the quantitative theory of Brillouin scattering in opaque materials by using Green's function methods. The work by Loudon [1.15, 1.16], Subbaswamy and Maradudin [1.17], Velasco and Garcia-Moliner [1.18], Zhang et al. [1.20] and developments in the computational approach developed by Every et al. [1.19] for solving the free-surface Green's function problem played a key role in this understanding. Nizzoli and Sandercock [1.13] presented a discussion on the production of a Brillouin spectrum by both the elasto-optic coupling and the ripple-scattering mechanism as governed by the opacity of the material.

The theoretical aspects of SBS and various SBS experimental researches were found to be extensively covered in a number of texts and also in such texts as the many PhD studies undertaken on this topic. The PhD studies in particular, provided an easily accessible resource that guided one through the somewhat complex formalisms encountered and most importantly pointed one to other relevant literature. The studies carried out on fast-ion conductors by Ngoepe [1.25], the pioneering high-temperature work by Stoddart [1.1; 1.3] and the groundbreaking high-pressure measurements by Crowhurst [1.4; 1.26] are but a few of such examples.

Chapter 2

SBS Experimental Method

2.1 Outline

An overview of the SBS experimental technique will be presented in this chapter. Brillouin scattering provides a description of the inelastic scattering of light from thermally induced acoustic waves. A resolution of the weak inelastically scattered light from the very intense elastic component forms a basic thrust of the SBS technique. This resolution requires a specialised stable instrument that can readily deliver the necessary contrast for the inelastically scattered light to be measured.

The development, by Sandercock, of a multipass interferometer from a standard Fabry-Pérot interferometer resulted in an instrument with a high contrast [2.1] making the observation of the weak inelastically scattered light routinely possible.

The basic equipment requirement in any surface Brillouin scattering spectroscopy requires the following: an intense source of highly monochromatic light, a high resolution and high contrast spectrometer, a sensitive detector and a multichannel analyser.

Figure 2.1 shows a photograph of the SBS apparatus. Figure 2.2 provides a diagram of the external optics, the (3+3)-pass tandem Fabry-Pérot interferometer (TFPI) and the data collection equipment.

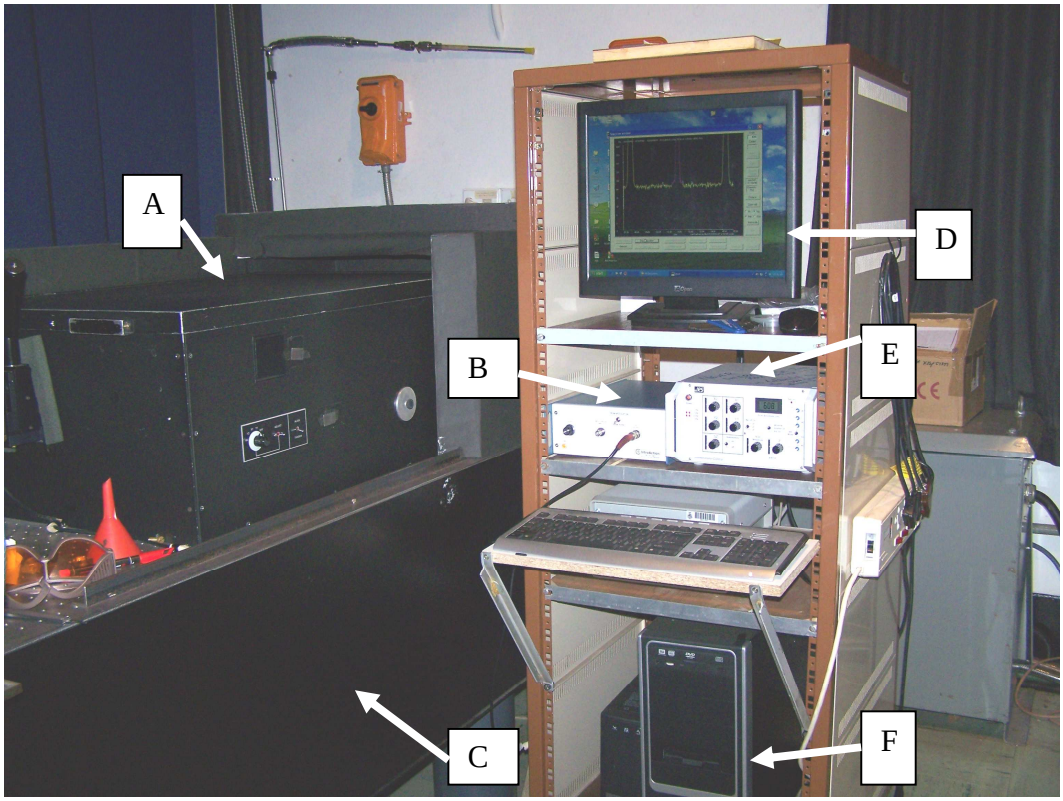


Figure 2.1: Photograph of the SBS apparatus.

Labels in the above figure are as follows:

A : The tandem Fabry-Pérot interferometer (TFPI) enclosed in a black metal box

B : The acousto-optic modulator (AOM) control unit

C : The optical table with the steel honeycomb core on top

D : The liquid crystal display (LCD) screen, multichannel analyser (MCA) output device

E : The TFPI control and stabilisation unit

F : Computer with the multichannel analyser (MCA)

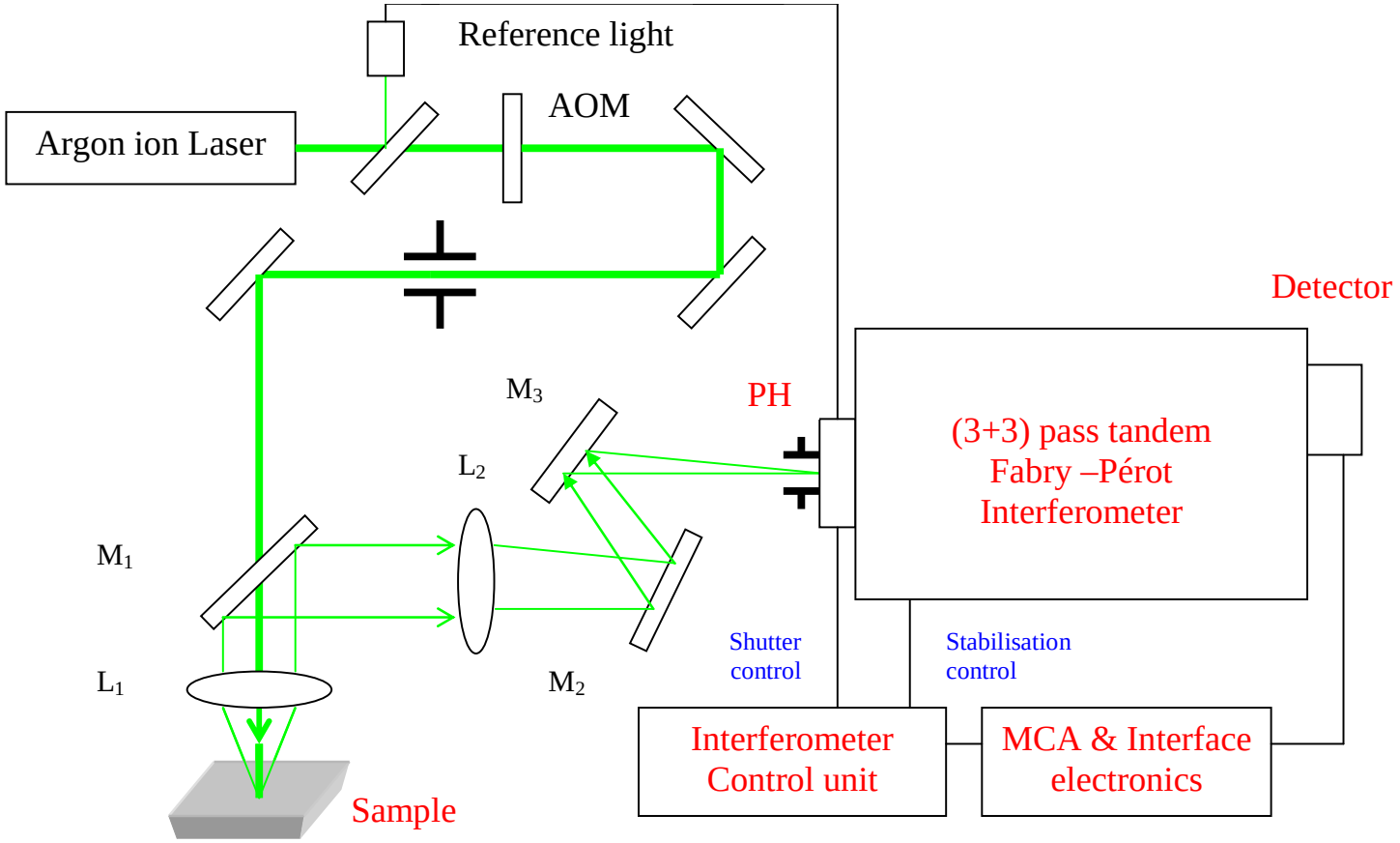


Figure 2.2: SBS configuration used in this work.

2.2 The laser

The laser provided the required source of highly monochromatic light for all light scattering experiments. Two water cooled argon ion lasers were used for the experiments at different phases, namely the 18 Watt Spectra-Physics model 171 laser and the 5 Watt Spectra-Physics model 2020 laser. The usage of argon as a laser medium and the process by which lasing, in argon ion lasers, occurs is well understood [2.2]. Depending on the decay scheme involved, argon ion system result in the emission of visible laser radiation that has a wavelength of between 450 and 530 nm. Whilst the frequency determines the laser power output, a number of transverse electromagnetic modes (TEM) may arise resulting in the modification of the power distribution across the beam. The true single mode (TEM_{00}) is the most useful; it gives a beam with a Gaussian intensity profile, minimum divergence and the smallest beam spot diameter [2.2]. The mode with a wavelength 514.5 nm was used for all measurements. To obtain the resolution required for SBS where the frequency shifts of the scattered light are in the range of a few GHz to about 150 GHz, a very narrow laser linewidth is required. From the broad gain profile of the laser as shown in figure 2.3, a single longitudinal mode is selected. A Spectra-Physics Model 583 temperature controlled intra-cavity etalon was used to achieve this. The etalon basically allows for the selection of a particular frequency whilst inhibiting all other oscillations. The alignment of the etalon results in a 50% drop in output power and adjusting the etalon temperature, thereby changing the optical path length leads to the selection of the desired TEM_{00} mode.

Depending on the arrangement of the auxiliary optics being used and the nature of the sample, the laser output power varied from about 400 mW to about 600 mW and the average incident laser power on the sample was about 55 mW as a result of losses associated with the auxiliary optics.

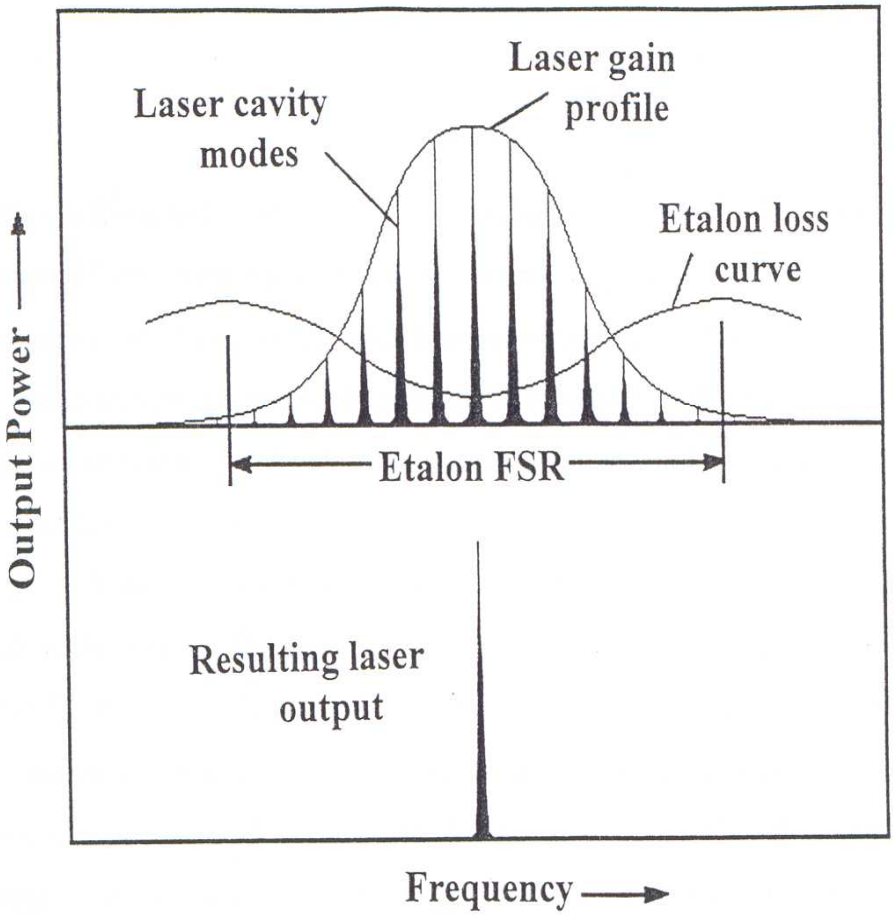


Figure 2.3: Etalon loss minimum coinciding laser gain maximum (after Operation Manual of Spectra-Physics Model 171 argon ion laser).

2.3 The tandem Fabry-Pérot interferometer (TFPI)

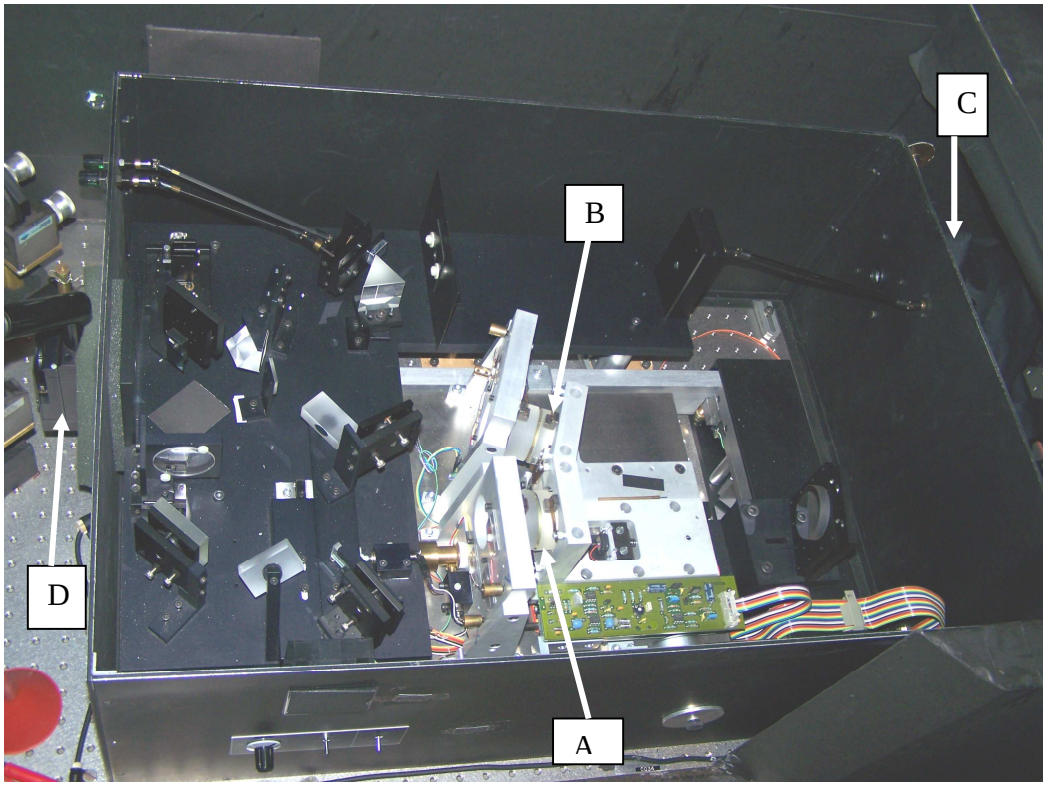


Figure 2.4: An aerial view of the JRS instruments (3+3) multipass interferometer, showing A - FP1, B – FP2, C – the detector (mounted on the TFPI box) and D – the shutter. { FP1, FP2 - Fabry-Pérot 1&2}.

The tandem Fabry-Pérot interferometer (TFPI) has had a significant impact in Brillouin scattering measurements due to its high resolution and large improvement in contrast. The frequency shifts of the scattered light in Brillouin scattering measurements are in the GHz range. High resolution implies the ability to measure signals that differ in frequency by very small values. High contrast implies the ability to discriminate signals of greatly different intensity while being close in frequency. The TFPI is therefore a very essential component of an SBS experimental arrangement.

In our laboratory we used the Sandercock-type (3+3)-pass Tandem Fabry-Pérot Interferometer fitted with a JRS Scientific Instruments vibration isolation system.

The first practical application of the multipass method was reported by Sandercock; in this case a beam was passed up to five times parallel to itself through a single interferometer [2.3]. The basic design of the TFPI is achieved by mounting two sets of parallel mirrors on the same translational stage. This configuration works as a tunable optical filter whose peak transmission is close to unity over a narrow spectral interval. In this case the ratio is set at $L_2/L_1 = 0.95$.

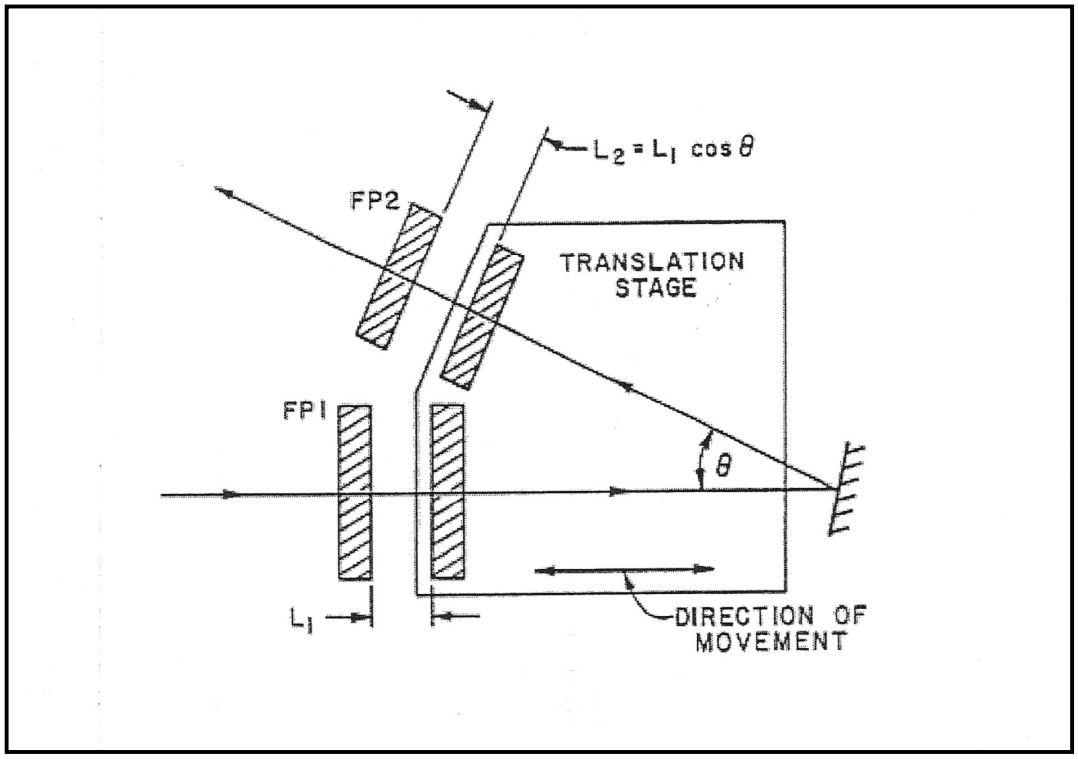


Figure 2.5: A plan view of the two Fabry-Pérot interferometers on a single translation stage (after Mock et al. [2.4]).

In the present work, the scattered light was passed (3+3) times i.e. 6 times through the interferometer achieving a contrast as high as 10^{11}. This contrast provided the capability to distinguish the weak inelastically scattered light from the intense elastically scattered light. Thus we were able to study weak acoustic phonon modes such as surface acoustic waves and observe the weak longitudinal and transverse thresholds of the Lamb continuum.

The TFPI is isolated from the surrounding disturbances as it is mounted on an active platform (JRS Scientific Instruments, Vibration Isolation System MOD - 2) that produces dynamic isolation. The TFPI is also located within a light tight box that rests on a steel honeycomb core on a thick optical table. High frequency vibrations are effectively damped by the design of the optical table.

During operation, a reference signal that is needed by the automatic alignment system is introduced with the aid of the JRS Scientific Instruments LM-2 shutter assembly. The reference signal is guided into the shutter assembly through an optical polariser to ensure suitable intensity of laser light for stabilisation.

2.4 The detector

The detector that was used for the measurements is an EG&G Optoelectronics Canada SPCM-200-PQ with a dark count of 1 per second. This detector is a silicon avalanche photodiode device with a high quantum efficiency being just over 44% for the 514.5 nm wavelength (see figure 2.6).

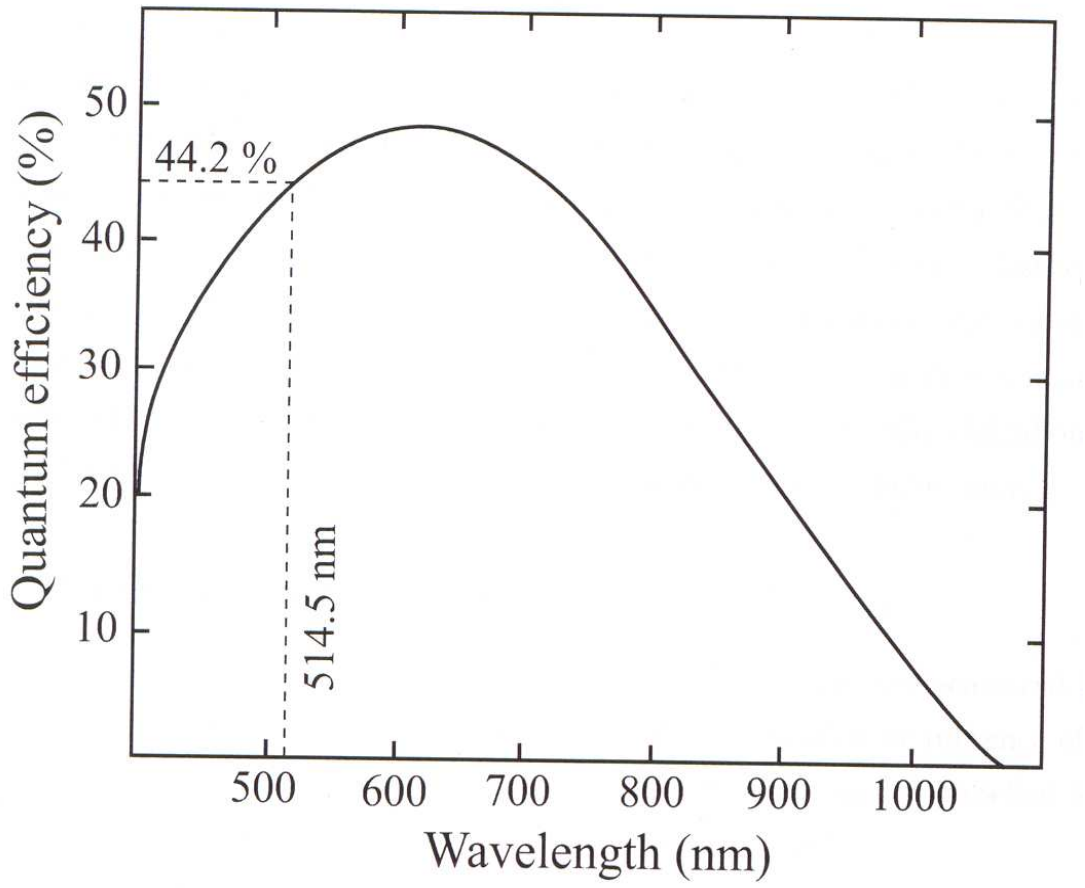


Figure 2.6: Photon detection efficiency for the SPCM-200-PQ detector [2.5].

The detector was also obtained from JRS Scientific Instruments and it was mounted directly on to the box that housed the TFPI.

2.5 The optical furnace

The optical furnace used for high temperature measurements is the one described in P.R. Stoddart's PhD thesis [1.1]. Figure 2.7 shows its main features.

Basically, samples were mounted inside the furnace on a recess that is ultrasonically drilled on the quartz rod. The quartz rod is inserted through the inclined arm located underneath the furnace and it is supported by a double O-ring fitting at a fixed angle of incidence of 70.9º. The heating element comprises a molybdenum wire with two tantalum heat shields around the element to reduce radiative heat losses. A Pt-Pt (13% Rh) thermocouple is placed a few millimetres from the sample to monitor the sample temperature. The SBS backscattering arrangement was realised through the fused quartz front window. The optical furnace was pumped down to a high vacuum of about 10^{-5} torr by a rotary pump backed by an oil diffusion pump. Ultra-pure argon (99.99%) was then bled in to a pressure of 18 mmHg to improve the thermal contact between the sample and the thermocouple.

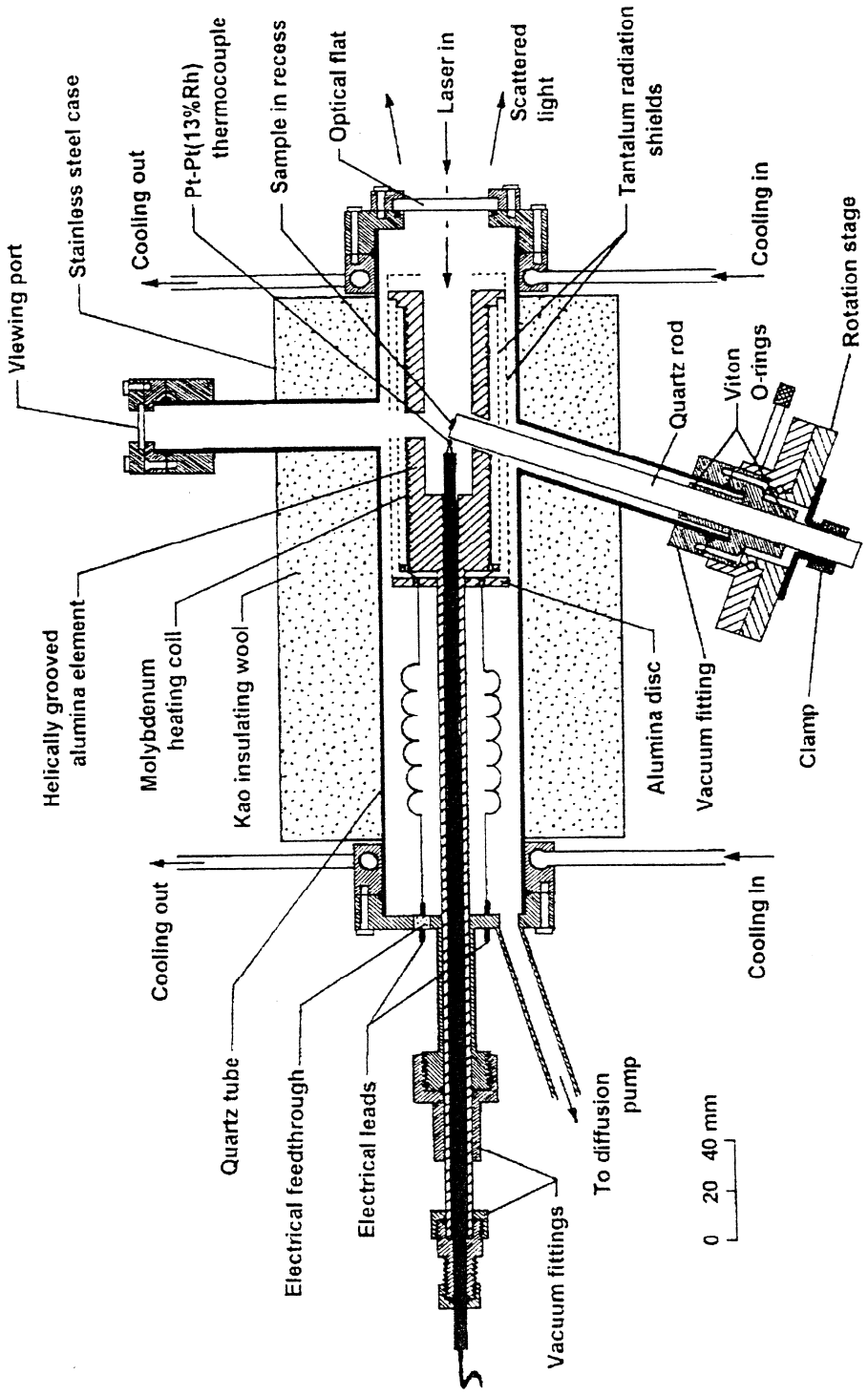


Figure 2.7: Cross section of the SBS optical furnace [1.1].

2.5.1 Temperature control

An auto-transformer (220V/10A) and Eurotherm 426 thyristor unit were used to power the heating element. A Eurotherm 818 temperature controller, shown in figure 2.8, was used to maintain the heating temperature with better than 1^{o}C stability. This kind of stability was of utmost importance especially during the typical long SBS measurements or spectrum accumulation periods, where there is a need to ensure that spectra are collected at the desired set-point temperature.



Figure 2.8: Eurotherm 818 temperature controller.

2.6 The multichannel analyser

All spectra were recorded by a Personal Computer based multichannel analyser (MCA) interfaced with the TFPI and the detector. During the course of this work two different MCA's were used namely a Nucleus Personal Computer Analyser PCA-II which was DOS based and a newer Windows based JRS Scientific Instruments Ghost multichannel analyser MCA - 1. This newer MCA was supplied with software for data analysis, spectrum calibration and curve-fitting. The spectrum calibration function was a most welcome development as this facilitated the acquiring of an SBS spectrum in terms of frequency shifts as opposed to channel numbers as was the case with the old MCA. Other functions were hardly used as spectra were always stored in ASCII format and later analysed using OriginLab software. When SBS spectra were acquired in terms of channel numbers, a computer program was coded in FORTRAN to calculate related frequency per channel calibration factors to enable the plotting of the spectra in terms of frequency shifts.

To obtain a spectrum of sufficient quality, up to 512 channels were used as this provided an acceptable interplay between acquisition time and resolution.

2.7 Daily setup for SBS measurements

The following discussion on the actual arrangement for the SBS measurements is based on the experimental configuration shown in figure 2.2.

Throughout the measurements a torch, rather than the main laboratory lights, was used for general illumination as the experiments are done in a darkened environment. Apart from avoiding a possible overload of the detector, the adjustment of the auxiliary optics for focusing was also another consideration.

For both the measurements on boron doped polycrystalline silicon and on the ternary semiconductor alloy $InAs_{0.91}Sb_{0.09}$, a 120 mm lens was used to focus the 514.5 nm laser beam onto the sample. To maintain a consistent arrangement during alignment leading up to the actual collection of the SBS spectrum, the boron doped polycrystalline sample was placed in the ultrasonically drilled recess in the sample holder of the high temperature optical furnace as shown in figure 2.7. All the measurements on the samples inside the high temperature optical furnace were carried out at a fixed angle of incidence of 70.9º.

The measurements on the ternary semiconductor alloy $InAs_{0.91}Sb_{0.09}$ were done with samples mounted on a specially machined sample holder fitted with a goniometer to enable the variation of both the angle of incidence and the azimuthal angle.

The 180º scattering (back scattering) geometry meant that the scattered light was collected by the same lens and eventually steered using mirrors M_2 and M_3 to the entrance pinhole of the TFPI. The steering has to be done carefully without changing the optical path-length as this might change the focus on the entrance pinhole. Using a simultaneous fine adjustment of the steering mirrors and the focal length, the image of the sample is projected onto a white card that is placed on the translation stage of the TFPI.

When carrying out these adjustments, light to the detector should be blocked and the detector should be switched off. Depending on the intensity of the scattered light from the sample, the setting on the acousto-optic modulator (AOM) can be adjusted; normally it was set at maximum. The AOM is used to adjust the intensity of the laser light; in this way the laser power source does not require any adjustment once the operating power has been set.

When the image on the white card shows a crisp pattern of bright spots against a dark background (a more granular look rather than a smeared out image), the focusing is at

its optimum and the possibility of obtaining a good spectrum from the TFPI is given a big boost.

The next step is the alignment of the TFPI as explained in the J.R. Sandercock Operator Manual for the tandem interferometer [2.6]. Figure 2.9 shows a typical output before and after optimisation with the TFPI in alignment mode.

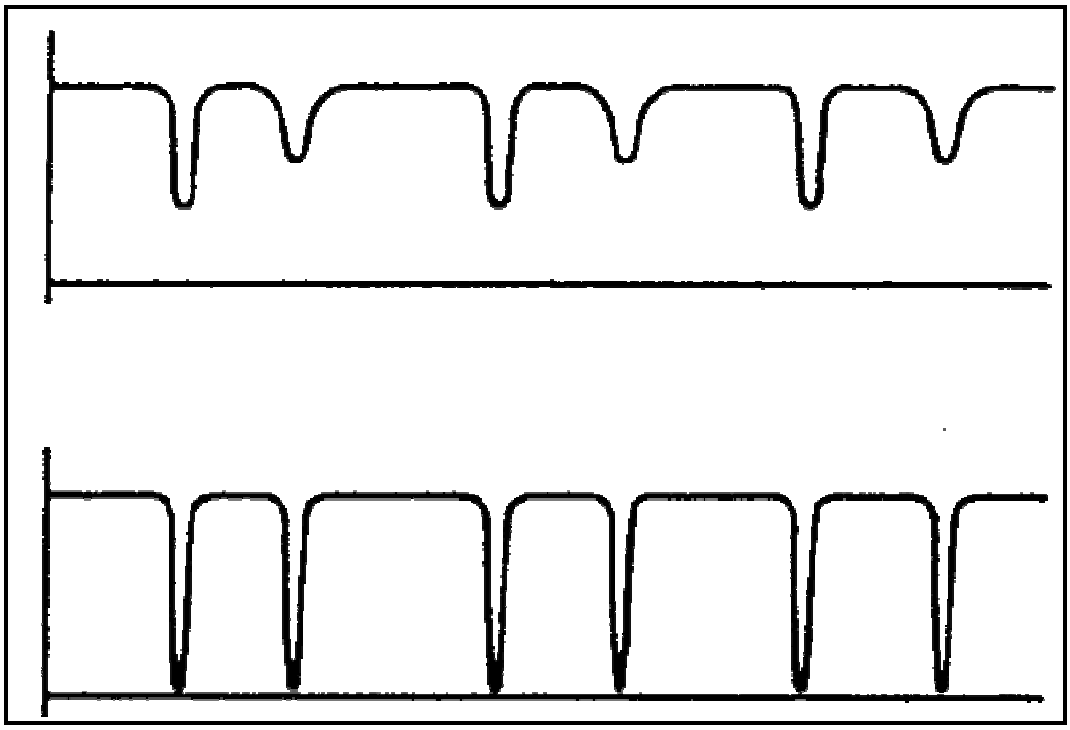


Figure 2.9: TFPI in alignment mode, before optimisation (top) and after optimisation (bottom) (from the JRS tandem interferometer operation manual).

After synchronisation is achieved, the system is switched over to the dynamic stabilizing control state. By so doing the control unit optimises all the settings: Δz, x_1 and y_1 for FP1 and x_2 and y_2 for FP2, to maintain maximum transmission. A reference signal of adequate magnitude is passed through an optical filter, via the shutter assembly to the TFPI to optimise stabilisation.

Depending on the aim of the measurement, a specific mirror spacing is chosen to calibrate the interferometer so that the measured frequency shift in channels is converted to frequency units. The additional aspect of selecting a particular mirror spacing for the measurements, is to enable the weaker surface wave position to be clearly separated from the very intense elastic peak. Consequently, a mirror spacing of either 2.5 mm or 4.0 mm was chosen for the measurements. A discussion on these matters has been provided by Sussner and Vacher [2.7]. However, a more condensed explanation can be found in the PhD studies referred to in Chapter 1.

When there was certainty that an optimal experimental setup has been reached either for the measurements inside the high temperature optical furnace or for the samples mounted on the specially machined sample holder, the collection of the SBS spectra was commenced.

Spectra for the boron doped polycrystalline silicon were collected from 20ºC to about 73.5ºC with the temperatures preset using the Eurotherm 818 temperature controller. A ramping rate of about 1ºC per minute was maintained between the fixed temperatures selected. Depending on the details of the features observed on the spectra, typical accumulation times ranged from about 12 hours to about 48 hours.

The average collection time for the SBS spectra of the ternary semiconductor alloy $InAs_{0.91}Sb_{0.09}$ was about 48 hours. Longer collection times were necessitated by the need to clearly distinguish the features of the Lamb Shoulder, on the collected SBS spectra.

2.8 Error analysis in SBS measurements

Sources of errors in SBS measurements are in general identified as follows:

- Instrumental errors - associated with the calculation of the frequency shifts of corresponding Brillouin scattering peaks. The error in calculating the frequency shift arises from the error in measuring the mirror spacing, the peak position of the ghosts and the Brillouin scattering peaks.

- Errors from scattering geometry - In SBS measurements, the scattered light to be analysed is collected by a large aperture collection lens due to the weak surface Brillouin scattering signal. The large collection aperture allows phonons with a range of wavevectors to contribute to the measured scattered light leading to the broadening of the phonon line shape thus introducing a systematic shift in the position of the peak.

- Errors from scattering cross section - In this case the scattering intensity as a function of scattering angle is considered. For the polarization in the sagittal plane (*p*-*p* polarization) of a backscattering geometry, the scattering intensity decreases for scattering angles (therefore angles of incidence) less than 40º or larger than 70º.

In this study, with due consideration to the error analysis given above, the setting of the mirror spacing in our instrument was made by adjusting a precision clock gauge to within (0.01 mm) or ± 10 μm when selecting a mirror spacing for our measurements, which was usually about 4 mm. In such a case an error of about 0.25% can result in the setting of the free spectral range (FSR). However, the accuracy of the SBS measurements was aided by calculating the arithmetic average of the Stokes and anti-Stokes frequency shifts to eliminate the error in the elastic peak position.

For increased scattering intensity in order to obtain better spectral features on the acquired SBS spectrum, the angle of incidence of about 70º was used for the SBS measurements in this work. For such typical configurations, the maximum error of measurement is less than 2% [1.1].

Above is a very brief description that is based on a more detailed qualitative and quantitative discussion on measurement precision in surface Brillouin scattering made by Stoddart [1.1] and expanded upon by Crowhurst [1.25].

Chapter 3

SBS of boron doped silicon

3.1 Introduction

Microelectromechanical systems (MEMS) are integrated micro systems or devices that combine electrical and mechanical functionalities. Their size typically ranges from micrometres to millimetres. MEMS technology is enabling new developments in the production of accelerometers, pressure, chemical and flow sensors, optical scanners, micro-optics and fluid pumps [3.1].

Boron-doped polycrystalline silicon is a widely used structural material in the manufacture of MEMS devices, transistors, solar cells, rectifiers and other electronic solid state devices [3.2, 3.3]. It is the increase in conductivity as a result of doping that allows more complex and high speed circuitry to be created. The performance and reliability of these devices, especially at elevated temperatures, requires a good understanding of the behaviour of their elastic properties.

Surface Brillouin Scattering (SBS) is a technique that is ideally suited for the determination of high temperature elastic constants, as it is a non-contact technique that allows the sample to be isolated, thereby avoiding the introduction of contaminants during measurements.

In this study, SBS is used to measure the elastic properties of boron-doped silicon from room temperature to about 74ºC. This range was of interest in this study as it corresponds to the temperature range of the functioning of some MEMS devices. Hence understanding to what extent, if any, are the mechanical properties of these

devices impacted by operating in this temperature range, becomes vital. A detailed study on the elastic properties of boron doped silicon at high temperatures i.e. 100ºC to 600ºC, is found in B.A. Mathe's PhD thesis [3.4].

Professor Linn W. Hobbs of the Department of Materials Science and Engineering at the Massachusetts Institute of Technology (MIT) USA supplied the samples that were studied.

3.2 Experimental Procedure

3.2.1 Sample preparation

Samples of about 16 mm^2 with a 50 micron thick epilayer deposited on each side of a high purity Si (001) substrate wafer were supplied. Both epilayers were doped with boron at about 3000 ppm (~10^{19} atoms per cm^3). In preparing the samples according to our sample holder specifications, about 4×4 mm, they were fractured with cleavage planes roughly along <110> and with [001] normal to both surfaces.

The surfaces of the samples were checked with the aid of a magnifying glass to see if they were of a suitable quality for SBS measurements. It was found that one side had a mirror-like finish suggesting less surface damage. This requirement is paramount in any SBS measurements; rough surfaces contribute to an increase in elastically scattered light making the measurement of the frequency shifted inelastic light extremely difficult. Moreover, rough surfaces cause a shift in the surface wave velocity, which would need to be corrected for. The relation of the frequency shift of a surface wave to the scale of surface roughness has been established by Eguiluz and Maradudin [3.5].

Preparing a sample for SBS measurements meant first cleaning the surface to be measured with acetone and then placing it in the sample recess of the quartz rod that was inserted into the optical furnace (see figure 2.7). The optical furnace was then evacuated to less than 10^{-5} Torr. To minimise chances of having contaminants in the optical furnace, it was repeatedly flushed with argon and evacuated again to about the same vacuum level. The procedure outlined in section 2.7 was then followed to align the sample for SBS measurements to commence.

3.2.2 Sample characterisation

With a 50 micron thick epilayer deposited on a high purity Si (001) substrate, it was initially anticipated that there would be appreciable variation of the Rayleigh SAW velocity from the [100] direction. The determination of the surface anisotropy was carried out given the dependence of phase velocities on propagation direction discussed in section 1.2.4. SBS measurements of the dependence of the Rayleigh SAW velocity on the azimuthal angle were carried out at a scattering angle of 70.9º.

Measurements of the Rayleigh velocity were taken in 10º intervals from an arbitrary starting point of 140º through to 330º. The aim was to collect spectra over a range of 180º with the intention of establishing high symmetry crystal directions.

The angular dispersion of the Rayleigh SAW velocity exhibited very weak anisotropy (see figure 3.1). The average Rayleigh SAW velocity was found to be 4598 $m.s^{-1}$ with a maximum deviation from this average value being about 13 $m.s^{-1}$.

This very weak anisotropy meant that a check whether the sample was amorphous or polycrystalline had to be made before detailed SBS spectra could be measured. In an effort to understand the reasons for the weak anisotropy, given that silicon (Si) is an anisotropic crystal, Raman measurements were carried out using a Jobin-Yvon T64000 triple grating spectrograph in triple additive mode.

From the observed line-shape in figure 3.2, it was established that we were measuring a p-type polycrystalline silicon. We concluded that we were not dealing with an amorphous sample as this would have shown a very broad Raman peak. However, in this instance a Raman peak, though not as sharp as the one for single crystal silicon, was observed. The Raman spectrum showed the characteristic asymmetry of the line-shape associated with p-type doping of polycrystalline silicon, known as the Fano line-shape. Several studies have been carried out on this phenomenon and these are highlighted by Mathe [3.4] in his studies of the same sample at high temperatures.

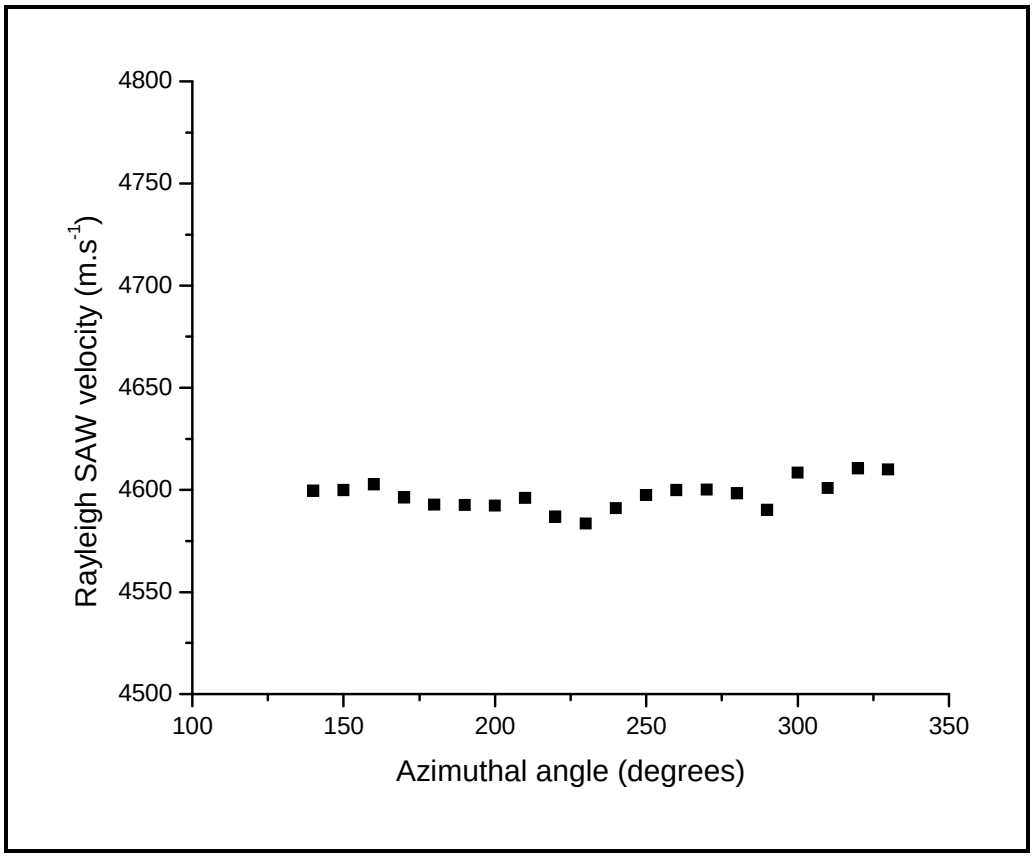


Figure 3.1: Angular dispersion of the Rayleigh surface acoustic wave (SAW) velocity on boron doped silicon.

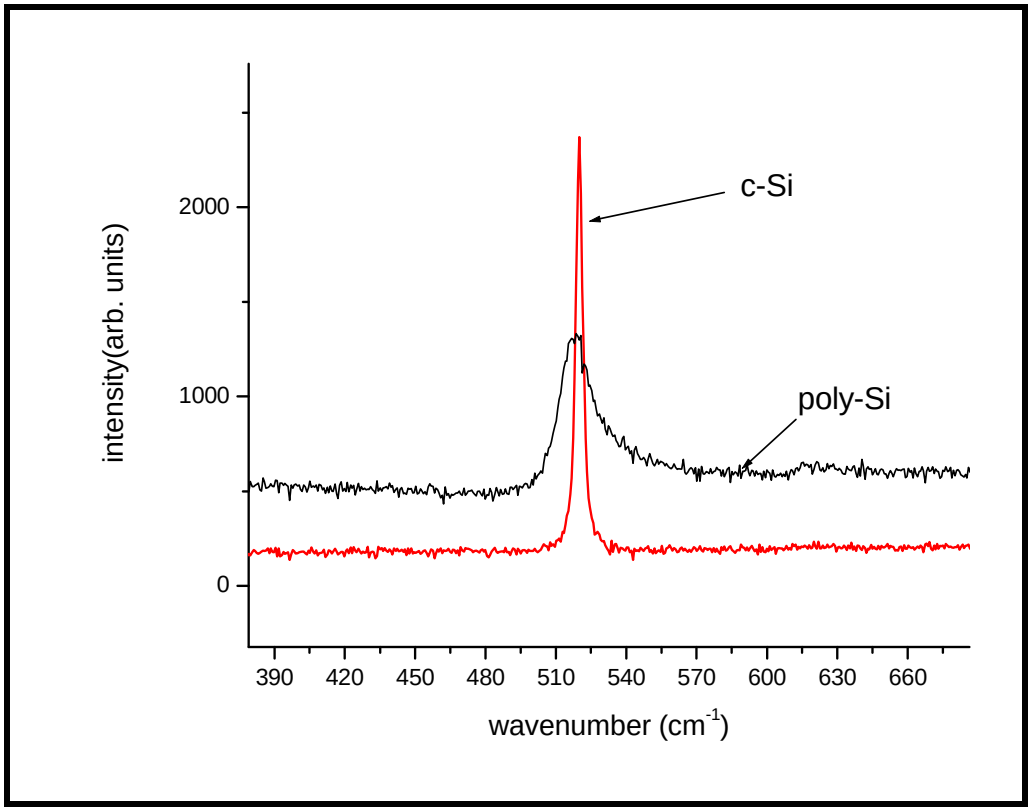


Figure 3.2: A Raman spectrum of boron doped polycrystalline silicon compared to that of crystalline silicon.

3.3 Results and Discussion

In figure 3.3, a typical surface Brillouin scattering spectrum for boron doped polycrystalline silicon is shown. The spectrum was acquired with a scan amplitude of 1.82 thereby excluding the instrumental ghosts with the aim of seeing clearer spectral features. Apart from the central peak at zero frequency shift that corresponds to the intense elastically scattered light and the Rayleigh SAW, shown as a set of two prominent peaks at ±16.8 GHz, the other spectral features of the Lamb shoulder were at times difficult to identify.

These are shown more clearly in figure 3.4 where the longitudinal threshold in the Lamb shoulder can be readily read off the spectrum.

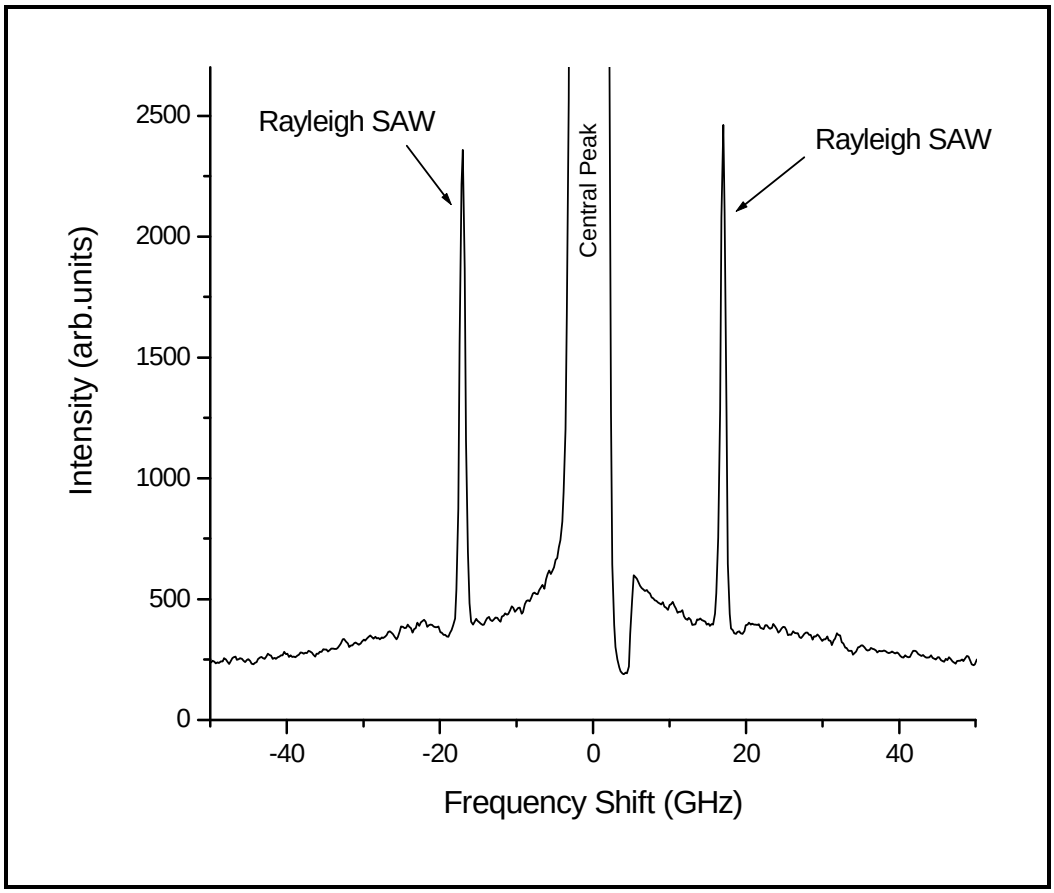


Figure 3.3: The SBS spectrum for boron doped polycrystalline silicon at 55.6ºC at a scan amplitude of 1.82, mirror spacing of 2.5 mm and the angle of incidence of 70.9º.

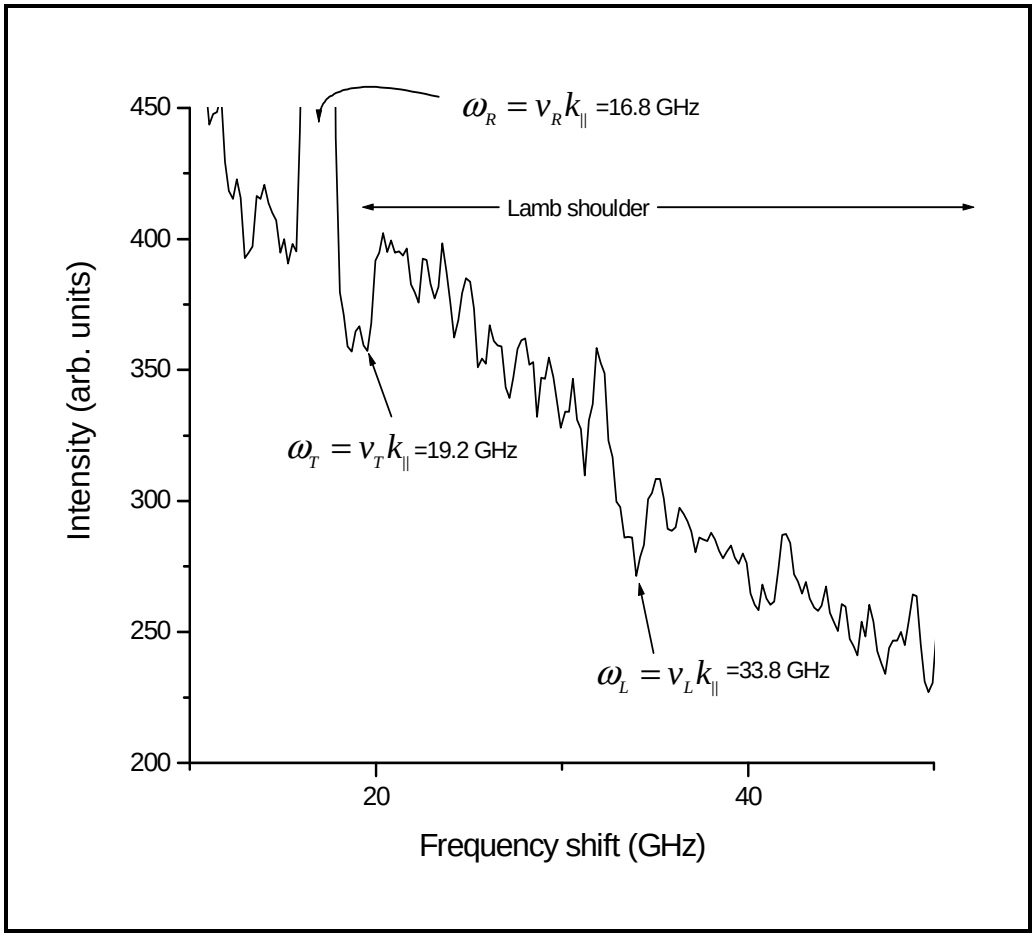


Figure 3.4: The anti-Stokes component of the SBS spectrum for boron doped polycrystalline silicon at 55.6ºC showing the frequencies $\omega_T = v_T k_{||}$ =19.2 GHz and $\omega_L = v_L k_{||}$ =33.8 GHz for the transverse and longitudinal thresholds respectively and also the frequency $\omega_R = v_R k_{||}$ =16.8 GHz for the Rayleigh surface acoustic wave (SAW). The angle of incidence is fixed at 70.9º.

The frequency shifts are obtained by fitting Lorentzian functions on to the Rayleigh SAW (RSAW) peaks on the relevant SBS spectrum. Noting the broadened peak as opposed to the theoretical delta function for the RSAW peaks, the deviation from the central value defined by the delta function can then be calculated from the determined Full Width at Half Maximum (FWHM) for each peak. The FWHM provide a measure of uncertainty in the measured acoustic velocities. The error analysis discussed in

section 2.8 has in general meant that an overall error of about 2% is mostly found in SBS measurements. In this measurement there was a 1.5% difference between the frequency at the centre of the peak and the one at the FWHM.

The isotropy of the sample meant that the values retrieved from the acquired spectra included only the Rayleigh SAW velocity and the longitudinal velocity associated with the frequency shift of the longitudinal threshold. The measured values are given in table 3.1.

Table 3.1: Measured Rayleigh SAW velocities (V_{RSAW}) and Longitudinal velocities (V_L) for selected temperatures.

Temperature (^oC)	Rayleigh SAW velocity ($m.s^{-1}$)	Longitudinal velocity ($m.s^{-1}$)
20.0	4581	9252
43.0	4632	9194
55.6	4633	9194
62.5	4623	9194
73.5	4620	9021

From the above table, effective elastic constants, C_{11} and C_{44}, can then be calculated for the isotropic boron doped polycrystalline material. The elastic constant C_{12} is then obtained from the relation for isotropy, $C_{12} = C_{11} - 2C_{44}$. Taking ρ, the density, as 2.332 g/cm^3 [3.6], the elastic constant C_{11} is readily obtainable from

$$C_{11} = \rho V_L^2 \qquad (3.1).$$

The longitudinal velocities are calculated from the measured frequency shifts on the SBS spectrum. One has to be cautious when reading off these values as the longitudinal thresholds may not always be 'nicely defined dips'. The longitudinal velocities in Table 3.1 above were read off the SBS spectrum to an accuracy of about 0.5 GHz.

With the C_{11} value calculated for each temperature, a computer program was coded in FORTRAN to solve equation (1.19), shown again below, in order to obtain the related C_{44} value.

$$\rho V_{RSAW}^2 - \left(\frac{C_{11}}{C_{44}} \times \frac{C_{44} - \rho V_{RSAW}^2}{C_{11} - \rho V_{RSAW}^2} \right)^{\frac{1}{2}} \times \left(C_{11} - \frac{\left(C_{11} - 2C_{44}\right)^2}{C_{11}} - \rho V_{RSAW}^2 \right) = 0$$

The input parameters in this equation are the C_{11} values, the density and the velocity of the Rayleigh SAW. As can be seen from the above equation, the only unknowns in the equation are C_{11} and C_{44}. So the coding involved finding an exact solution for C_{44} after obtaining C_{11} from equation (3.1). The measured elastic constants C_{11}, C_{12} and C_{44} are presented in table 3.2.

Table 3.2: Measured elastic constants C_{11}, C_{12} and C_{44} for boron doped polycrystalline silicon.

Temperature (^{o}C)	C_{11} **(GPa)**	C_{12} **(GPa)**	C_{44} **(GPa)**
20.0	199.6	85.8	56.9
43.0	197.1	80.3	58.4
55.6	197.1	80.3	58.4
62.5	197.1	80.9	58.1
73.5	189.8	73.2	58.3

Most often the elastic constants of such MEMS devices are given in terms of engineering elastic moduli namely, the Young's modulus and the bulk modulus. Therefore using equations (1.9) and (1.12) these elastic moduli have been calculated from the SBS measurements as shown in table 3.3.

Table 3.3: Measured elastic moduli for boron doped polycrystalline silicon for the 20°C to 73.5°C temperature range.

Temperature (°C)	Bulk modulus (GPa)	Young's modulus (GPa)
20.0	123.7	148.0
43.0	119.2	150.6
55.6	119.2	150.6
62.5	119.6	150.0
73.5	112.1	149.1

The graphs of the variations of the elastic moduli with temperature are presented in figures 3.5 and 3.6. The error bars indicate the error in the measurement of the velocities of about 1.5%.

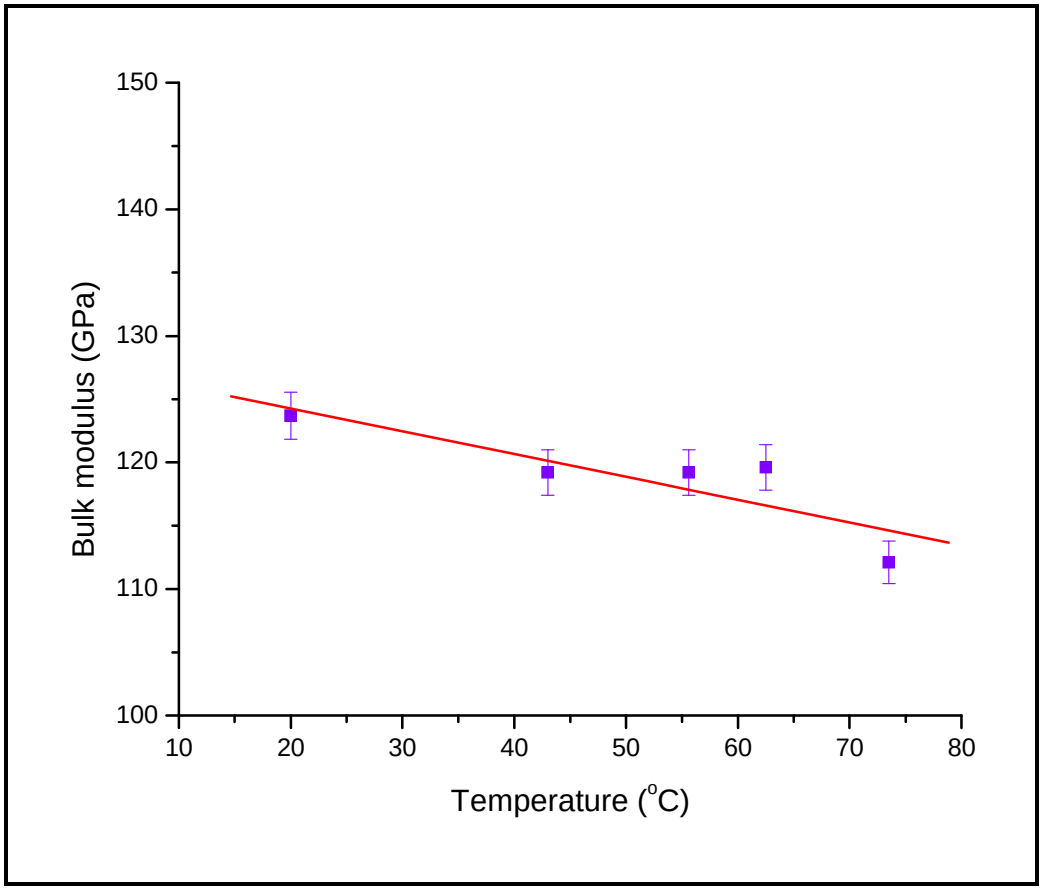


Figure 3.5: Variation of the bulk modulus with temperature for boron doped polycrystalline silicon.

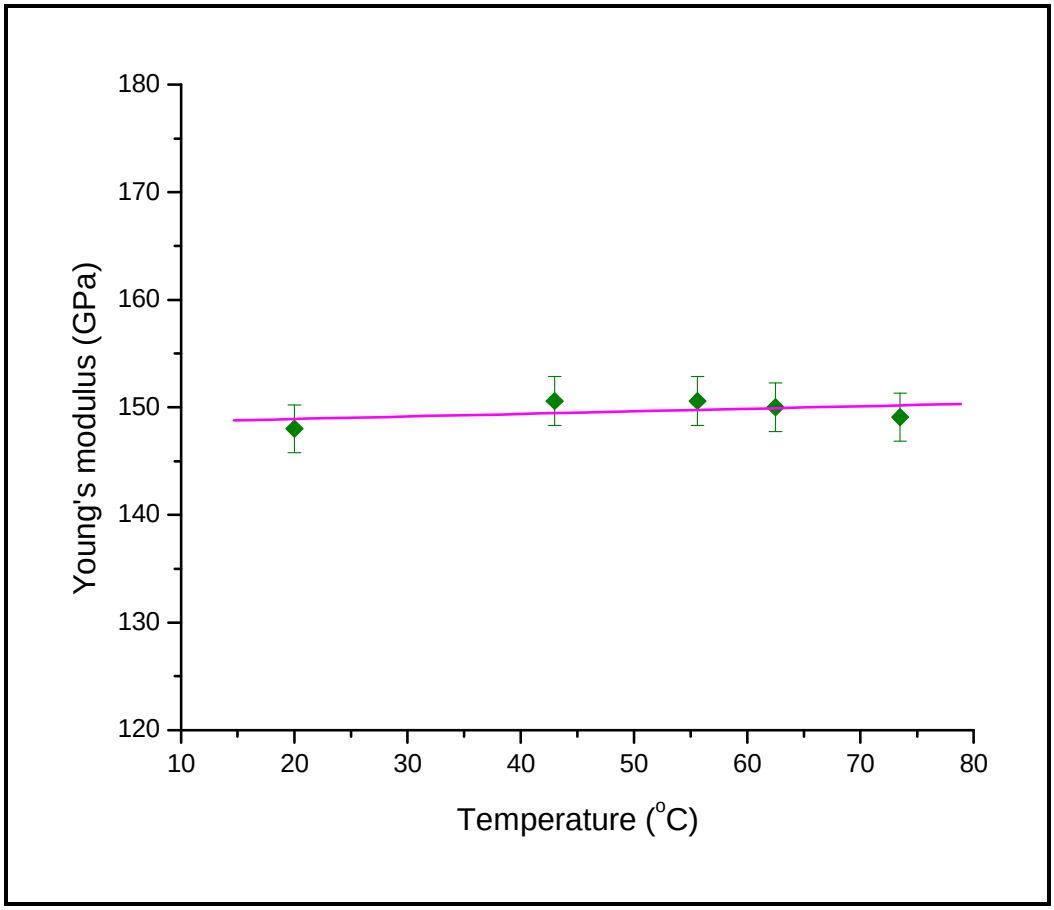


Figure 3.6: Variation of the Young's modulus with temperature for boron doped polycrystalline silicon.

3.4 Conclusion

In the temperature range from room temperature to about 74ºC, the Young's modulus of boron doped polycrystalline silicon is fairly stable at a value of about 150 $\pm$ 2 GPa (see Figure 3.6) while on the other hand, the bulk modulus shows a linear decrease from about 124 GPa at 20ºC to a about 112 GPa at 73.5ºC (see Figure 3.5). The room temperature measurements yielded a Poisson's ratio of 0.30.

A literature search for the value of the Young's modulus of polycrystalline silicon can yield values ranging from 140 GPa to about 210 GPa. So, one needs to be careful when an attempt is made at comparing these values, as some of these values could be for undoped polycrystalline silicon or for some other particular dopant or the fabrication of the material could be different. For example, Sharpe Jr. et al. quote a figure of 169 GPa for phosphorus doped polycrystalline silicon [3.3].

A factor that seems to be significant is the actual characterisation of the material as being polycrystalline. It would be instructive to establish whether the polycrystalline material is composed of randomly distributed grains or has some preferred texture.

The Young's modulus value of 150 ± 2 GPa obtained for our sample suggests that it has a (100) preferred texture. In Greek et al. [3.7], reference is made to studies that have shown that polycrystalline silicon with a (100) preferred texture has a Young's modulus of 149 GPa. However, they presented a calculated Young's modulus value of 162.7 GPa by using averages of elastic compliance constants which are then weighed with relevant texture measured by XRD and then added up.

Considering the calculations of the elastic constants C_{11}, C_{12} and C_{44} for polycrystalline silicon with a random distribution done by Anastassakis and Liarokapis [3.8] where they averaged the Voigt and Reuss averages, the Young's modulus value of about 162 GPa was obtained. This value is higher than the value measured in the present work which again leads to a conclusion that we were not measuring a polycrystalline material with a random distribution of crystallites but one with preferred texture.

Even though we could not obtain detailed information about the fabrication of our sample, the information provided by the suppliers that the material comprised an epilayer of polycrystalline silicon deposited on each side of a high purity Si (001) substrate, is somewhat a contradiction of terms. One would expect an epilayer to have

the orientation of the substrate. It is clear from our observation that the material used in our investigation is polycrystalline but there are strong indications of preferred texture.

Chapter 4

SBS measurements of $InAs_{0.91}Sb_{0.09}$

4.1 Introduction

The need to improve the fabrication process, the performance and reliability of optoelectronic devices has been a major driving force in the study of the optical, electrical and mechanical properties of the III-V semiconductors. Therefore, the characterisation of these semiconducting materials plays an important role in evaluating technical production factors in order to optimise the production process. Additionally, it is very important to understand how their mechanical properties are influenced by the fabrication process and how these mechanical properties are affected during operation. Understanding how mechanical properties are affected can be done by taking a closer look at the material's elastic properties. The measurement and monitoring of the material's elastic constants in a variety of environments, is a key factor in understanding its elastic properties. Surface Brillouin scattering is a technique well suited to the study of the mechanical properties of these semiconducting materials.

Semiconducting alloy materials made from elements of groups III and V on the periodic table, have been used in varied optoelectronic devices such as lasers, photodetectors and optical gas sensors. For these purposes, both binary and ternary alloys have been produced. Studies have been carried out on III-V ternary semiconducting materials as viable replacements for HgCdTe [4.1 – 4.3]. Considering the III-V ternary alloys, $InAs_{1-x}Sb_x$ has become an important focus in the development of long-wavelength optoelectronic devices due its possible room temperature band gap ranging from about 0.17 to 0.35 eV [4.4]. Furthermore, this

alloy is reported to have high electron mobility making its application in high speed devices very attractive [4.5].

The alloy with a composition x = 0.09 is receiving increasing attention [4.6] as it has a room temperature energy gap corresponding to a wavelength of about 4.2 μm which is within the infrared wavelength range 3-5 μm, the transmission window in the atmosphere, where long-range detection is of interest.

The elastic constants of the III-V binary semiconductors have been extensively measured but little information for the III-V ternaries is available. To the best of our knowledge there is no report to date on the measurement of the elastic constants of the ternary alloy $InAs_{0.91}Sb_{0.09}$.

In this study, the SBS technique was employed to measure the room temperature elastic constants of the $InAs_{0.91}Sb_{0.09}$ ternary alloy which are essential in furthering the understanding of the mechanical properties of devices that are fabricated from such alloys.

4.2 Sample preparation and characterisation

$InAs_{0.91}Sb_{0.09}$ samples with dimensions of about 4×4 mm were supplied by Professor J.R. Botha and his research group at the Nelson Mandela Metropolitan University (NMMU) in Port Elizabeth, South Africa. These undoped samples with a mirror-like finish were grown by atmospheric pressure metalorganic vapour phase epitaxy (MOVPE-grown) on an InAs substrate. Further information sent with the ternary alloy is that it was measured to be about 2.7 μm thick by the Nomarski differential interference method and was lattice matched to the (100) orientation of the InAs substrate.

A Laue X-ray analysis of the ternary alloy was carried out to confirm the (100) orientation. The Laue method is mainly used to determine the orientation of large single crystals. The preferred crystal orientation is determined from the position of the spots on the Laue photograph. Each spot can be indexed, i.e. attributed to a particular plane, by using relevant standard charts.

The Laue X-ray photograph of the $InAs_{0.91}Sb_{0.09}$ sample that was studied is shown in figure 4.1. The photograph was compared to standard charts for different crystal orientations and based on the standard (100) projection chart for cubic crystals (see figure 4.2); the sample surface was indeed determined to be (100).

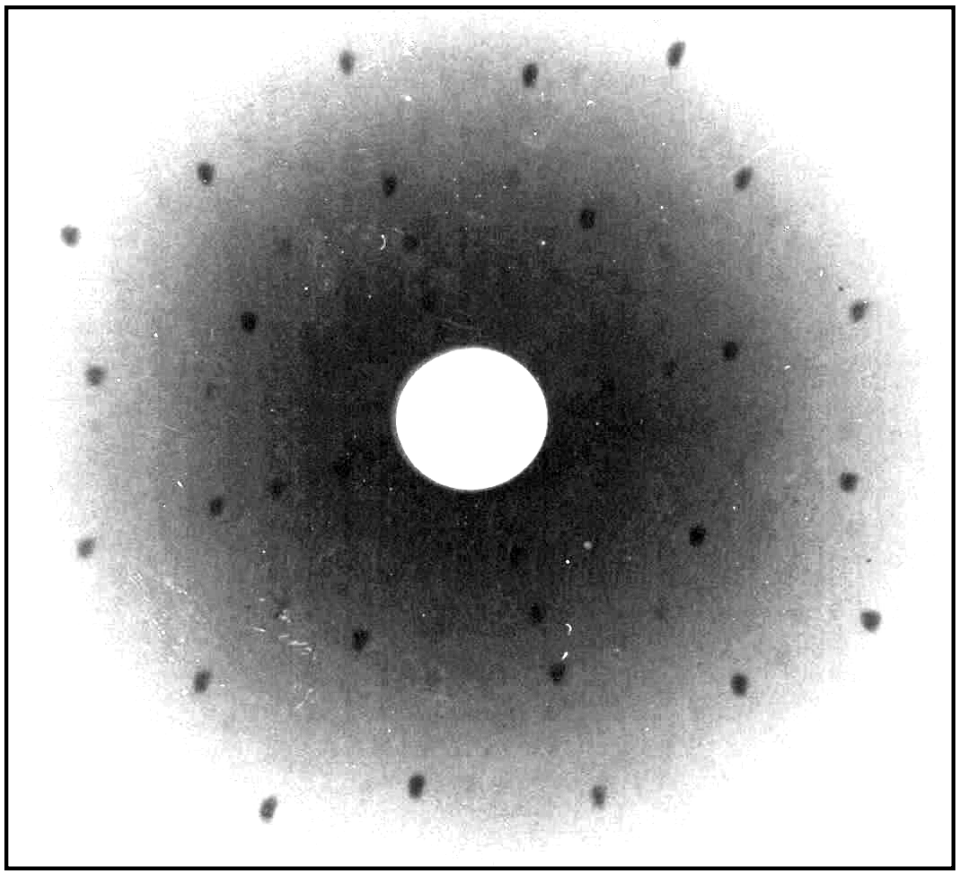


Figure 4.1: Laue X-ray photograph of $InAs_{0.91}Sb_{0.09}$ revealing the (100) orientation.

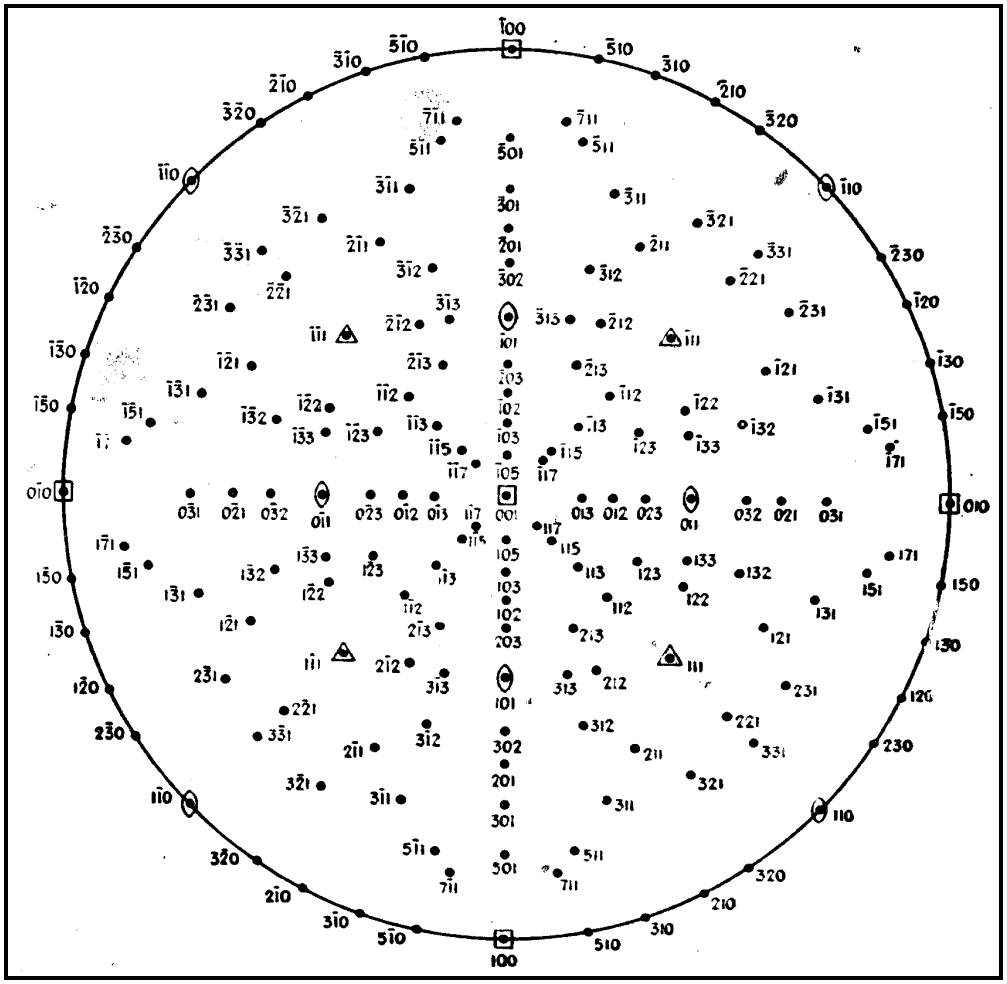


Figure 4.2: An example of a standard (100) projection for cubic crystals.

In Chapter 1, it was shown that the determination the elastic constants of a material requires the knowledge of the material's mass density. Therefore an X-ray diffraction measurement was carried out on the sample to determine its lattice constant. The measurement was done at room temperature using a Philips PW1050 diffractometer (Cu Kα radiation at 40kV and 20 mA). From the X-ray diffraction measurements, the lattice constant was determined to be 6.0811 Å. The density was then calculated from the lattice constant and the total atomic weight in the unit cell.

The ternary semiconductor alloy $InAs_{0.91}Sb_{0.09}$, as with a number of III-V compounds, forms a crystal with a cubic zinc-blende structure. Noting that there are four formula units per unit cell for zinc blende structures, the density was calculated as,

$$\rho = \frac{1.66 \times Z \times F}{V} \qquad \text{g/cm}^3 \qquad (4.1)$$

where Z is the number of formula units in a unit cell, F is the formula weight, V is the volume of the unit cell measured in Å^3 and 1.66 is derived from Avogadro's number. The formula weight F was calculated using atomic weights in the following way:

F = 114.80 g/mol (for In) + 91% of 74.92 g/mol (for As) + 9% of 121.80 g/mol (for Sb) = 193.94 g/mol. The density was found to be 5.729 g/cm^3.

SBS measurements were commenced after the sample's surface was cleaned with alcohol and acetone to maintain its mirror like finish.

4.3 SBS technique on $InAs_{0.91}Sb_{0.09}$

The experimental arrangement follows the one detailed in section 2.7. It was mentioned then that instead of an optical furnace as with the boron doped polycrystalline sample, the ternary semiconductor alloy $InAs_{0.91}Sb_{0.09}$ sample was mounted on a specially machined sample holder that is fitted with a goniometer to enable the variation of both the angle of incidence and the azimuthal angle. Further, the measurements in this case were only done at room temperature. For the calibration of the spectrum, the interferometer mirror spacing was set at 4.0 mm throughout the measurements. These measurements were carried out using the refurbished TFPI and the new JRS Scientific Instruments Ghost multichannel analyser MCA - 1. This meant that the SBS spectrum on the output of the MCA was now displayed in terms of frequency shifts and not channel numbers.

4.3.1 Variation of the Rayleigh SAW

The determination of the surface anisotropy was also carried out for this sample. SBS measurements of the dependence of the Rayleigh SAW velocity on the azimuthal angle were carried out at a scattering angle of 71º. For the (100) plane of a cubic crystal, measurement over at least 90º of the sample surface is sufficient. In this case measurements were done for the full 360º range at 10 degree intervals with the aim of seeing how the Rayleigh SAW behaved and also to see the periodicity of the variation. It can be seen in figure 4.3 that there is a clear 90º repeat interval in the variation of the Rayleigh surface acoustic wave (SAW) with the azimuthal angle. Seeing that we had an anisotropic cubic crystal, it was important to establish the [001] and the [011] symmetry directions. This choice is based on the discussion in Chapter 1 section 1.2.4 where explicit secular functions that determine the surface and longitudinal wave speeds in the [001] and [011] crystallographic directions are introduced. With the aid of the dispersion curve in figure 4.3, the [001] direction was found to be corresponding to the position given by the 100º position on the dispersion curve by fitting a cosine curve to the data points. The [011] direction could then be located at 45º from this 100º position.

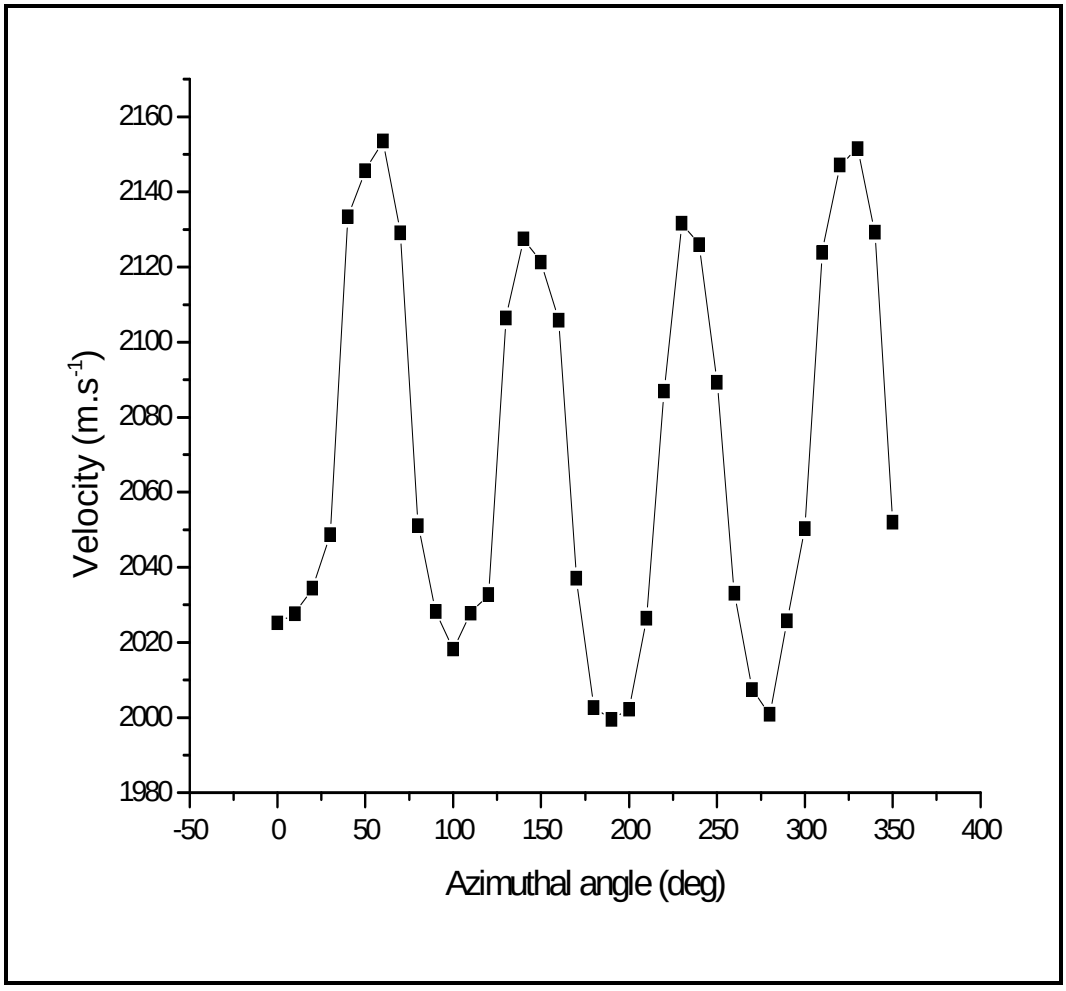


Figure 4.3: The variation of the Rayleigh SAW on the (100) surface of the single crystal $InAs_{0.91}Sb_{0.09}$ showing a 90º repeat interval.

4.3.2 Recovery of elastic constants

The values of the elastic constants C_{11}, C_{12} and C_{44} were recovered from the SBS measurements taken in the [001] and the [011] directions. Figure 4.4 shows a typical SBS spectrum acquired for this material. It took about 48 hours to acquire this spectrum and what is of note here are the clearly defined longitudinal and transverse thresholds of the Lamb continuum. The spectrum collection time and the excellent manner in which the TFPI and the auxiliary optics were aligned resulted in the acquiring of such spectra with well defined features. The shape of the central peak is modified by the shutter that removes the elastically scattered light while introducing a reference signal for the purpose of maintaining the alignment of the interferometer.

The HWHM (half width at half maximum) measurements of the Rayleigh SAW velocities were found to be about 54 $m.s^{-1}$. This value gave a difference of about 2.5% between the velocity measured from the frequency shift at the centre of the peak and the one measured from the frequency shift at HWHM. The SAW velocities are listed in Table 4.1.

The spectral features of the Lamb shoulder for the [001] and the [011] directions are shown in figures 4.5 and 4.6 respectively. The key feature is the longitudinal threshold that will later be utilised in the direct calculation of the elastic constant C_{11}.

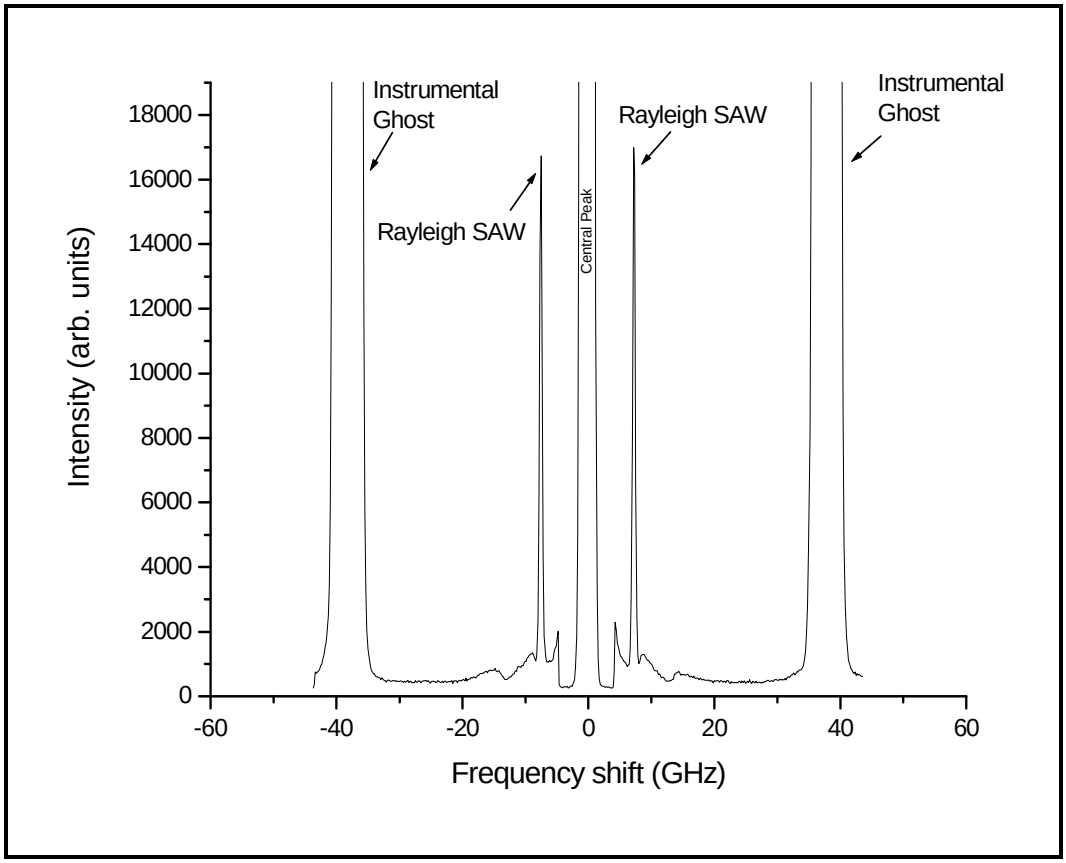


Figure 4.4: A typical SBS spectrum of $InAs_{0.91}Sb_{0.09}$ measured at an angle of incidence $\theta_i = 71°$. The dominant peak arises from the Rayleigh SAW, the longitudinal minimum of the Lamb shoulder can be clearly seen. The shape of the central peak is modified by the shutter that removes the elastically scattered light while introducing a reference signal for the purpose of maintaining the alignment of the interferometer.

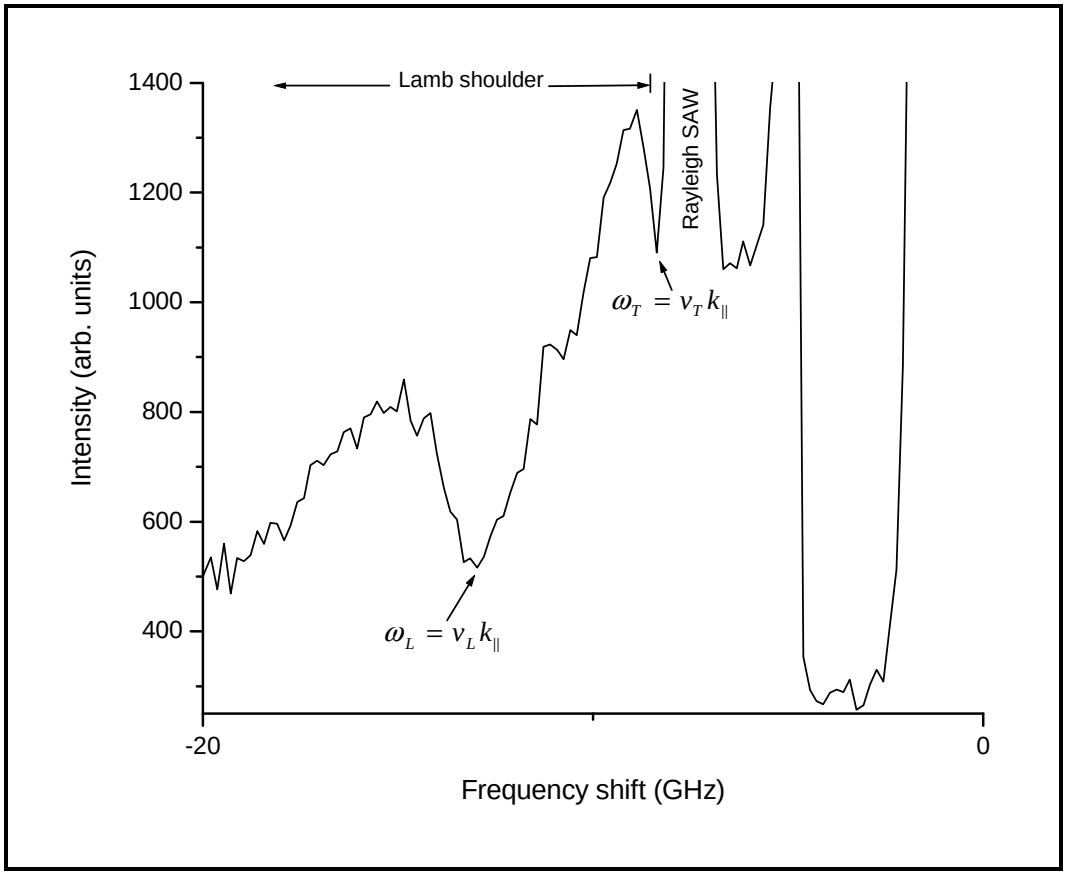


Figure 4.5: The measured Stokes component of the SBS spectrum on an enlarged scale, of $InAs_{0.91}Sb_{0.09}$ for the [001] direction on the (100) surface. The Rayleigh SAW, the transverse threshold $\omega_T = v_T k_{||}$ and the longitudinal threshold $\omega_L = v_L k_{||}$ can be clearly seen. The spectrum was acquired at a scattering angle of 71º.

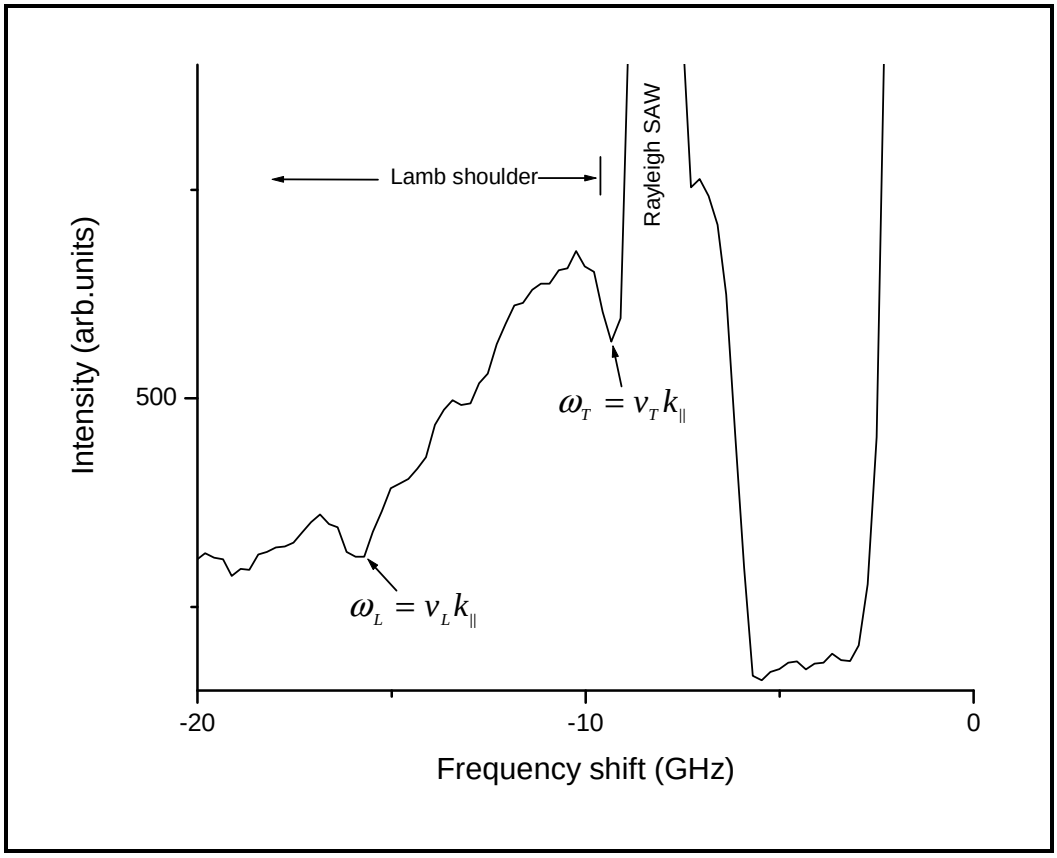


Figure 4.6: The measured Stokes component of the SBS spectrum on an enlarged scale, of $InAs_{0.91}Sb_{0.09}$ for the [011] direction on the (100) surface. The Rayleigh SAW, the transverse threshold $\omega_T = v_T k_{||}$ and the longitudinal threshold $\omega_L = v_L k_{||}$ are shown. The spectrum was acquired at a scattering angle of 71º.

The positions of the minima in the respective Lamb shoulders corresponded to the longitudinal thresholds thereby making it possible to obtain required frequency shifts for the calculation of the longitudinal velocities V_L. To find the surface acoustic wave (SAW) velocities, Lorentzian functions were fitted to the SAW peaks to locate the central values of the frequency shifts. From the measured frequency shifts equations (1.4) and (1.20) in Chapter 1 can then be used to find the required velocities as shown in table 4.1.

Table 4.1: Measured SAW and Longitudinal threshold frequency shifts and their corresponding velocities for the (100) surface of the ternary semiconductor alloy $InAs_{0.91}Sb_{0.09}$.

	[001] direction		**[011] direction**	
	FREQ. SHIFT (GHz)	VELOCITY ($m.s^{-1}$)	FREQ. SHIFT (GHz)	VELOCITY ($m.s^{-1}$)
SAW	7.39	2011	7.86	2139
Longitudinal	12.80	3483	15.36	4179

The relation between surface acoustic phase velocities and elastic constants was highlighted in the discussions in chapter 1. In this case we have measured 4 velocities and there are 3 parameters (i.e. C_{11}, C_{12} and C_{44}) to be determined – this is an over determined problem that is solved by a fitting procedure. One approach would be to do a least squares fit to the 4 velocities. This would require in particular, the cubic equations (1.17) and (1.18) to be solved and the correct root (of three) to be selected each time.

We have however adopted a much simpler approach to the fitting, which avoids the necessity of solving the cubic equations. We do this by taking the merit function to be

$$\chi^2 = (h_1^2 + h_2^2) + w\left(h_3^2 + h_4^2\right) \qquad (4.2)$$

where w is the relative weighting factor for the longitudinal velocities as compared with the Rayleigh SAW measurements and h_1, h_2, h_3 and h_4 are defined as follows

$$h_1 = \rho V_{RSAW}^2 - \left(\frac{C_{11}}{C_{44}} \times \frac{C_{44} - \rho V_{RSAW}^2}{C_{11} - \rho V_{RSAW}^2} \right)^{\frac{1}{2}} \times \left(C_{11} - \frac{C_{12}^2}{C_{11}} - \rho V_{RSAW}^2 \right) \tag{4.3}$$

$$h_2 = \rho V_{PSAW}^2 - \left(\frac{C_{11}}{C_{44}} \times \frac{C_{44} - \rho V_{PSAW}^2}{\left\{ \frac{1}{2}\left(C_{11} + C_{12} + 2C_{44} \right) \right\} - \rho V_{PSAW}^2} \right)^{\frac{1}{2}}$$

$$\times \left(\frac{1}{2}\left(C_{11} + C_{12} + 2C_{44} \right) - \frac{C_{12}^2}{C_{11}} - \rho V_{PSAW}^2 \right) \tag{4.4}$$

$$h_3 = \rho V_L^2 - C_{11} \tag{4.5}$$

$$h_4 = \rho V_L^2 - \frac{1}{2}\left(C_{11} + C_{12} + 2C_{44} \right) \tag{4.6}$$

where h_1, h_2, h_3 and h_4 are secular functions that determine the surface and longitudinal lateral wave speeds in the [001] and [011] crystallographic directions which for a perfect fit would all be zero.

The quantities h_3 and h_4 correspond to the deviation of the squared longitudinal velocities from their measured values and h_1 and h_2 are not very different from being the deviation of calculations from squared measured SAW velocities.

In the calculation of the elastic constants, the SAW velocities were given a bigger weighting than the longitudinal velocities. This is largely due to the possibility of locating the centre of the SAW peaks by fitting Lorentzian functions whilst on the other hand the longitudinal thresholds presented themselves more as somewhat rounded valleys rather than sharp dips. This can be clearly seen in figures 4.5 and 4.6. Given this factor of a greater uncertainty in measuring the longitudinal velocities, a

weighting factor of $w = 0.25$ was assigned to the longitudinal velocities in the calculation of the merit function χ^2.

The measured and calculated velocities are compared in table 4.2 following the minimisation of χ^2.

Table 4.2: Measured and calculated velocities (with a V_L weighting of 0.25) for the (100) surface of the ternary semiconductor alloy $InAs_{0.91}Sb_{0.09}$.

	[001] V_{RSAW} **(m/s)**	**[011]** V_{PSAW} **(m/s)**	**[001]** V_L **(m/s)**	**[011]** V_L **(m/s)**
Measured	2011	2139	3483	4179
Calculated	1984	2156	3587	4087
% deviation	1.37	0.77	2.98	2.19

On minimisation of χ^2 the fitted values of the elastic constants were found to be:

$C_{11} = 73.7 \pm 1.3$ GPa

$C_{12} = 40.4 \pm 0.9$ GPa

$C_{44} = 38.7 \pm 1.3$ GPa

The minimisation of χ^2 was also done with the values of the velocities obtained from the FWHM readings. The elastic constants obtained from this minimisation were then compared to the elastic constants obtained from the measured velocity values in table 4.2. The difference between these values is given as the error in the measurement of elastic constants C_{11}, C_{12} and C_{44} as shown above.

The SBS spectra were calculated from the determined values of the elastic constants C_{11}, C_{12} and C_{44} and compared with spectra measured in the [001] and the [011]

directions based on the assumption that the scattering is entirely by the ripple mechanism, and hence is proportional to $\frac{1}{\omega}\mathrm{Im}\left\{G_{33}\left(k_{\|},\omega\right)\right\}$. The comparison illustrated in figures 4.7 and 4.8 shows a good agreement between measured and calculated spectra particularly for the SAW modes. The uncertainty in locating exact positions of the longitudinal minima is evident when comparing the "valleys" of the measured spectra to the calculated "dips".

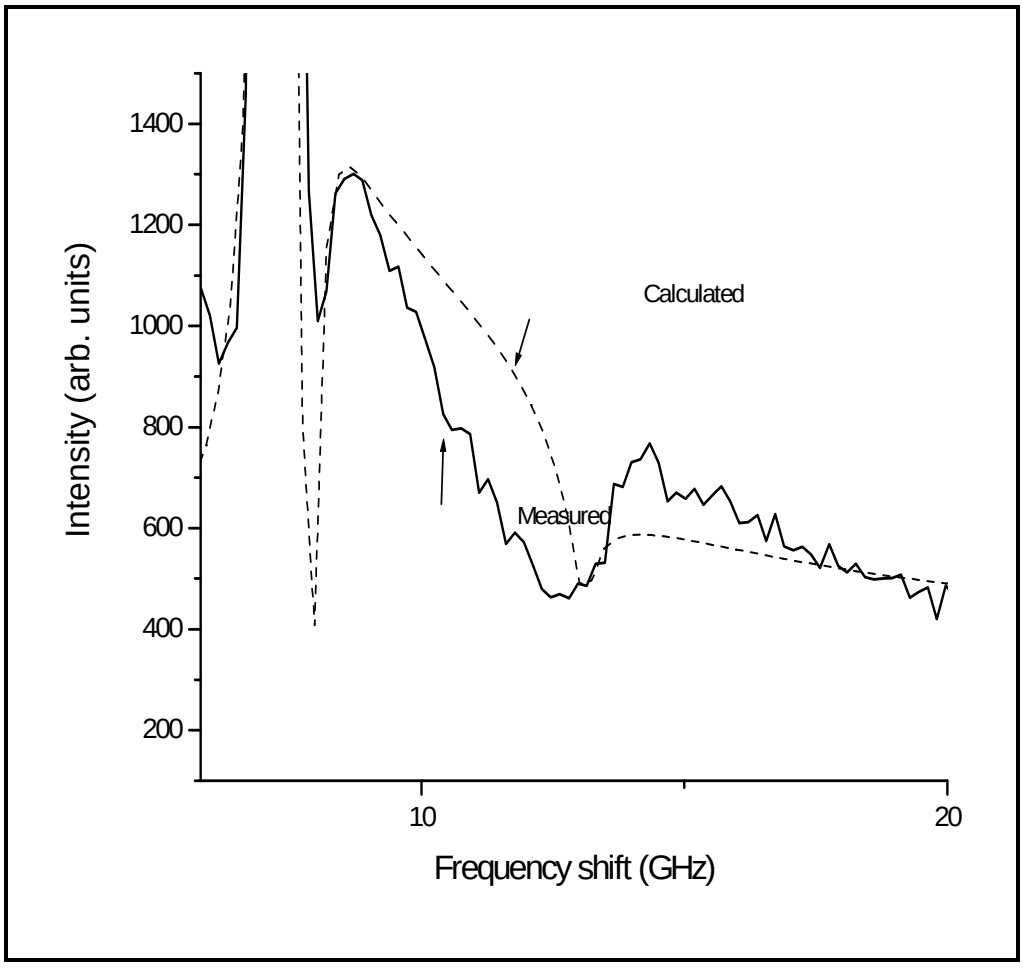


Figure 4.7: The measured and calculated SBS spectra for the [001] direction on the (100) surface of $InAs_{0.91}Sb_{0.09}$.

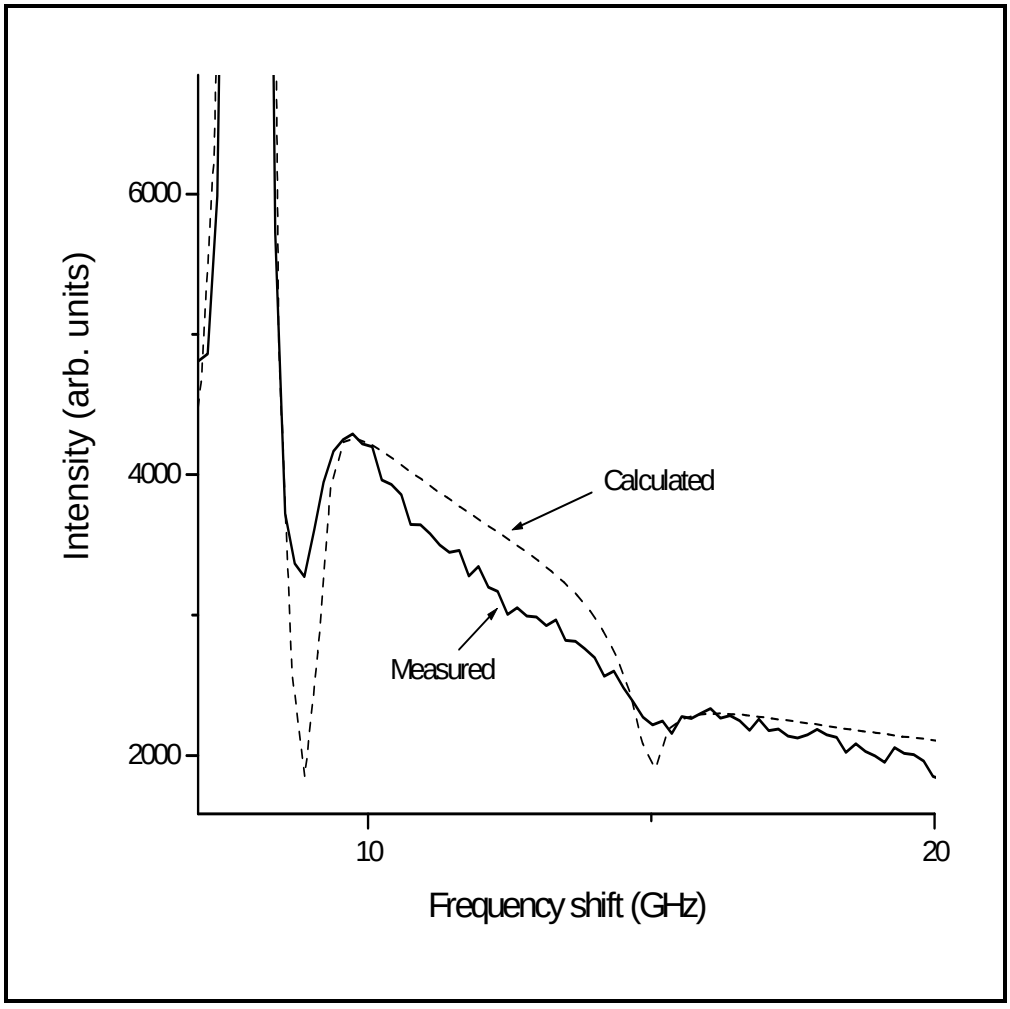


Figure 4.8: The measured and calculated SBS spectra for the [011] direction on the (100) surface of $InAs_{0.91}Sb_{0.09}$.

The approach to minimisation of the merit function χ^2 provides additional information on the accuracy of the measured elastic constants as shown in figures 4.9 to 4.11 which are contour plots of χ^2 in $(\text{GPa})^2$ for the variation of pairs of elastic constants with the third one kept fixed. The iterations give a minimum χ^2 value of about 13. The description of the observed covariance of the elastic constants is given below.

In figure 4.9, elastic constants C_{11} and C_{12} are allowed to vary while C_{44} is kept fixed. The minimisation of χ^2 shows an accurate determination of $(C_{11}-C_{12})$ and a less certain determination of $(C_{11}+C_{12})$ since χ^2 increases much more rapidly when $(C_{11}-C_{12})$ is varied than when $(C_{11}+C_{12})$ is varied.

In figure 4.10, the elastic constants C_{11} and C_{44} are allowed to vary while C_{12} is kept fixed. Here the contour plot shows a more accurate determination of $(C_{11}+C_{44})$ and a relatively less accurate determination of $(C_{11}-C_{44})$.

Lastly, in figure 4.11, the elastic constant C_{11} is kept fixed while C_{44} and C_{12} are allowed to vary. The minimisation of χ^2 shows that $(C_{44}-C_{12})$ is accurately determined while there is a less certain determination of $(C_{44}+C_{12})$.

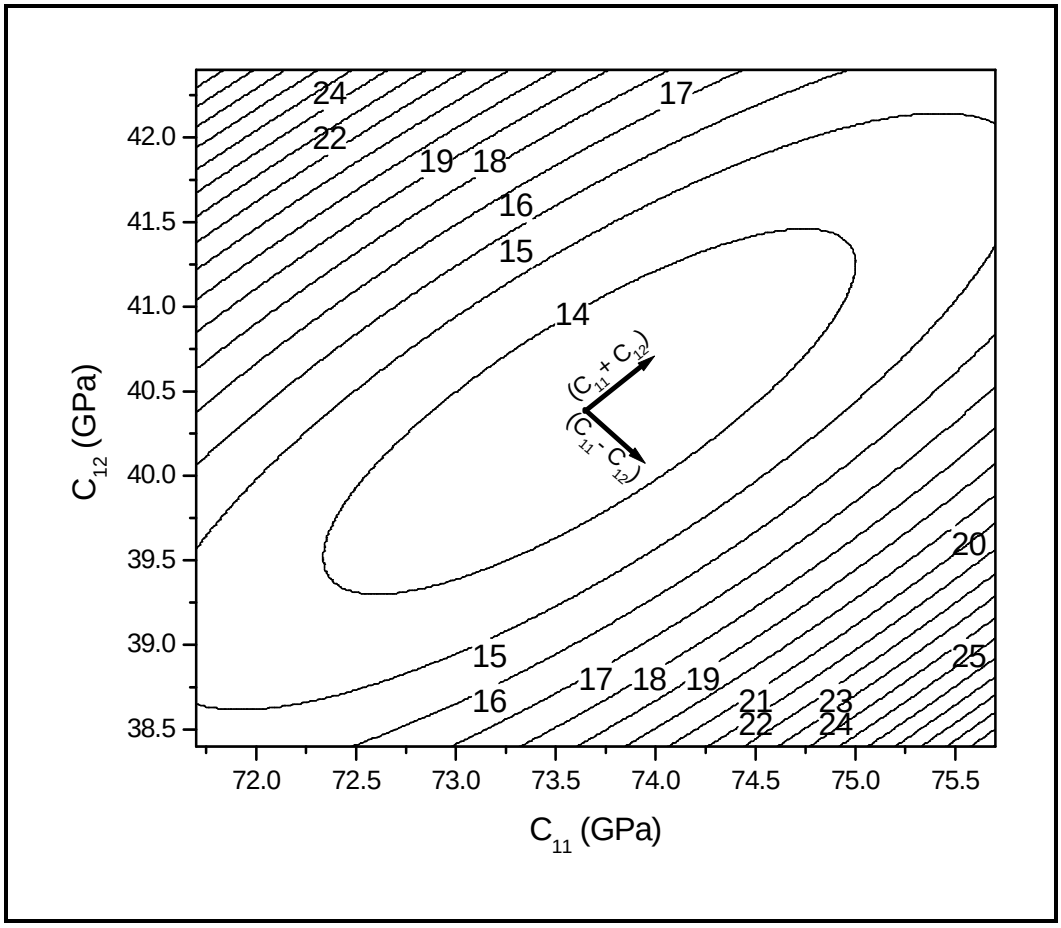


Figure 4.9: Contour plot of χ^2 in units of (GPa)^2 for variation of C_{11} and C_{12} whilst keeping C_{44} fixed at 38.7 GPa.

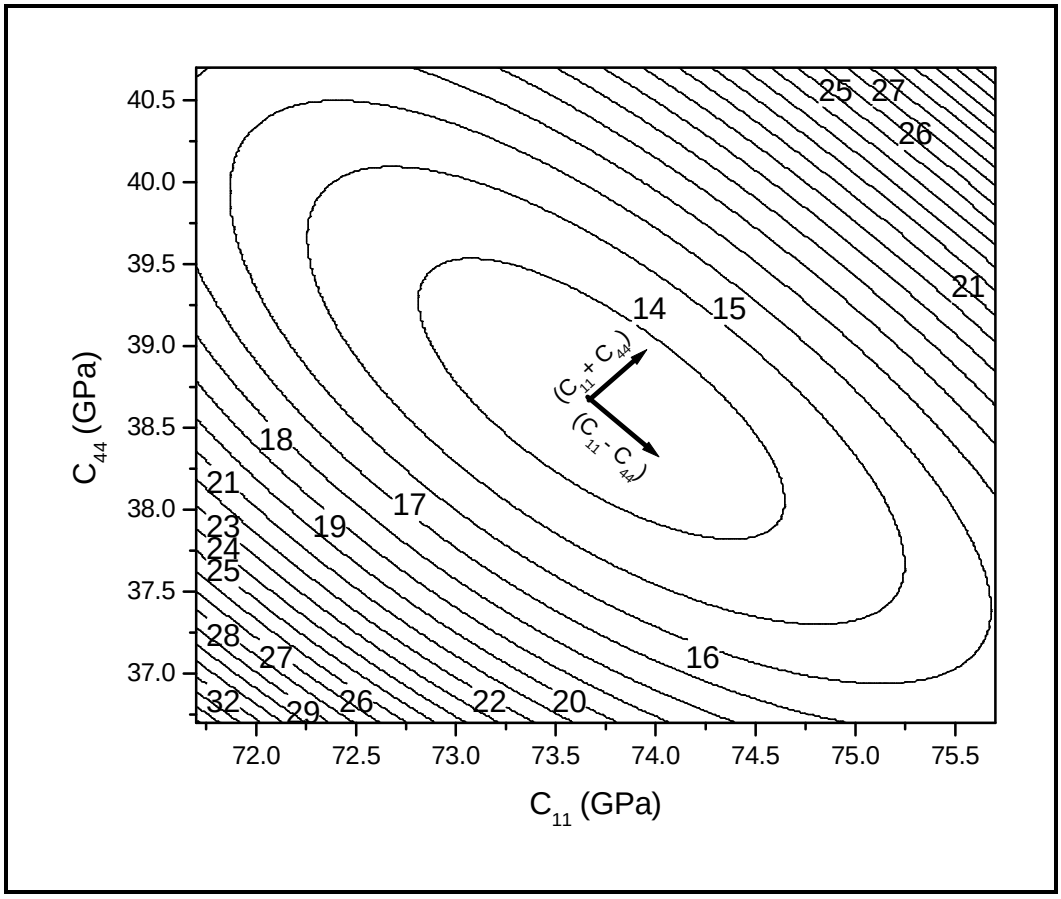


Figure 4.10: Contour plot of χ^2 in units of (GPa)^2 for variation of C_{11} and C_{44}, whilst keeping C_{12} fixed at 40.4 GPa.

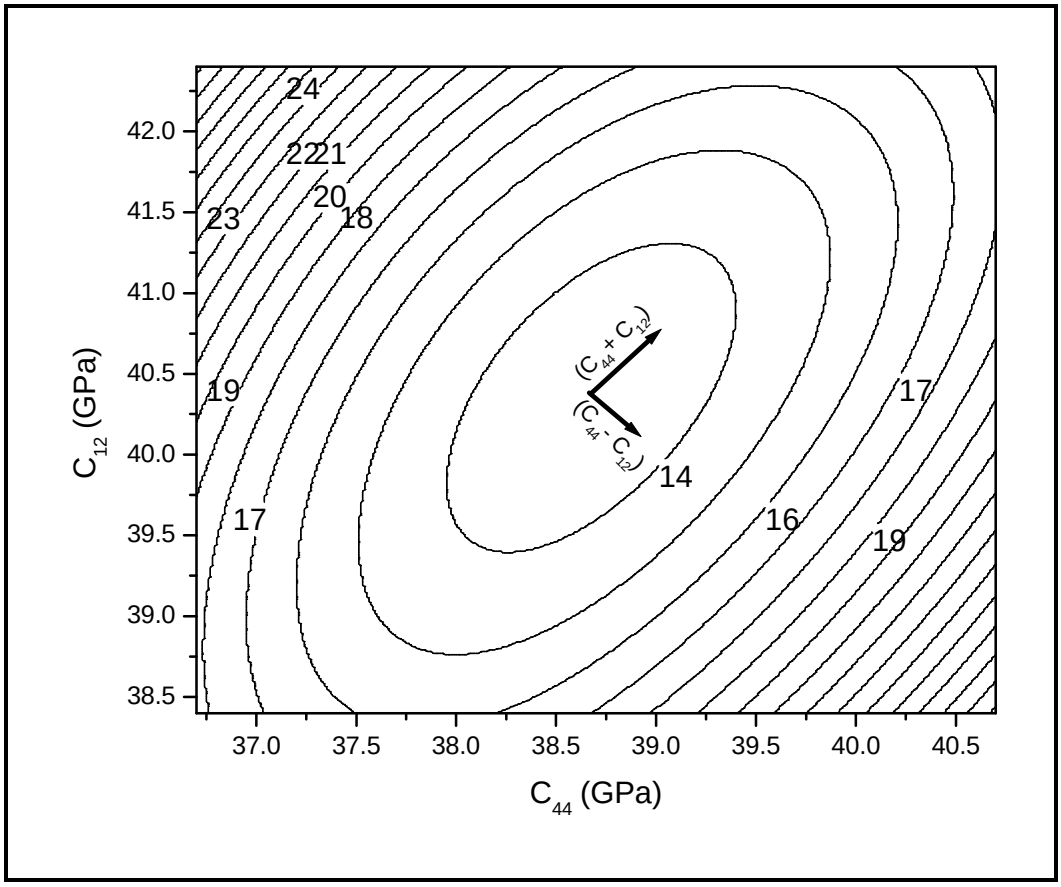


Figure 4.11: Contour plot of χ^2 in units of (GPa)^2 for variation of C_{44} and C_{12} whilst keeping C_{11} fixed at 73.7 GPa.

4.4 Conclusion

In this chapter, room temperature SBS measurements have been presented for the ternary semiconductor alloy $InAs_{0.91}Sb_{0.09}$. The Rayleigh SAW, pseudo-SAW and the transverse and longitudinal thresholds of the Lamb continuum were observed in the SBS spectra. The velocities of both the Rayleigh and the pseudo-SAW modes indicated a direction dependent behaviour when the angular dependence measurements were carried out on the sample.

A simple and robust fitting procedure was carried out for the recovery of the elastic constants. To obtain all three elastic constants, the positions of the Rayleigh SAW peak, the pseudo-SAW peak and the minimum in the Lamb continuum at the longitudinal threshold were measured. Measurements in the [001] and the [011] directions on the (100) surface of the ternary alloy $InAs_{0.91}Sb_{0.09}$ yielded four velocities that were used in the constructed merit function to determine the three unknown elastic constants.

Chapter 5

Conclusion

In this dissertation, we have employed surface Brillouin scattering to determine the elastic properties of two selected semiconducting materials. SBS is a non-contact, non-destructive technique that probes thermally excited acoustic phonons and as such is important in the characterisation not only of semiconducting materials but of all materials in general. In SBS, the population of surface excitations allowed by the sample geometry can be observed via the ripple or elasto-optic mechanism or both depending on opacity and can yield information on the elastic constant tensor of the material.

The preparation of samples for SBS measurements entailed the determination of the crystallographic orientation of the sample surface given that the phase velocities can depend on propagation direction.

The study on boron doped polycrystalline silicon entailed the solving of two equations for determining the two effective elastic constants C_{11} and C_{44} of this material presumed isotropic. Surface isotropy was established by measuring the angular dependence of the Rayleigh SAW velocity. When these measurements revealed a very weak anisotropy, Raman scattering was employed to assess the crystalline attributes of the material. It was established from these Raman scattering measurements that the material was polycrystalline.

The isotropy of the material meant that the values retrieved from the acquired SBS spectra included only the Rayleigh SAW velocity and the longitudinal velocity associated with the frequency shift of the longitudinal threshold. Having measured these two velocities, a direct method of determining the two effective elastic

constants was utilised making the traditional procedure of fitting theory to measured data to extract elastic constants unnecessary.

In measuring the engineering elastic moduli of boron doped polycrystalline silicon, the Young's modulus was a parameter that could readily be compared with other measured or theoretical values of the material. It was established that the measured Young's modulus value of 150 ± 2 GPa compares very well with values quoted for polycrystalline silicon with a preferred texture rather than for polycrystalline silicon with a random distribution of crystallites.

Surface anisotropy was observed in the ternary semiconductor alloy $InAs_{0.91}Sb_{0.09}$. The angular dependence of the surface acoustic wave speeds in this (100) oriented single crystal was measured and by so doing the [001] and [011] crystallographic directions were determined. The Rayleigh SAW velocity and the longitudinal velocity associated with the frequency shift of the longitudinal threshold were measured in the [001] crystallographic direction while the pseudo SAW velocity and the longitudinal velocity associated with the frequency shift of the longitudinal threshold were measured in the [011] crystallographic direction. This led to an over determined problem where we had 4 equations to solve for the 3 unknown elastic constants. A computer program was coded in FORTRAN to implement a fitting procedure for recovering elastic constants C_{11}, C_{12} and C_{44}. This was done by minimising a merit function constructed from explicit secular functions that determine the surface and lateral longitudinal wave speeds in the [001] and [011] crystallographic directions. In this calculation, the contributions of the lateral longitudinal wave speeds were given a smaller weighting factor because of the lesser precision with which they could be measured as compared to the SAW and PSAW values. To our knowledge this is the first time the elastic constants of $InAs_{0.91}Sb_{0.09}$ have been measured.

In this work, it was shown that SBS is a powerful technique in the probing of elastic constants of bulk semiconducting materials. The combination of the data of the SAW

modes and key points in the Lamb continuum, makes it possible to extract all elastic constants of bulk polycrystalline materials or bulk materials with cubic symmetry.

Our research group has developed expertise in using the SBS technique on different materials under different conditions. These include: bulk materials, thin films, multi-layers, high temperatures and high pressure conditions. With regards to the materials studied for this dissertation, Mathe [3.4] has already carried out studies on boron doped polycrystalline silicon at high temperatures (100ºC to 600ºC). Similarly, high temperature studies on the ternary semiconductor alloy $InAs_{0.91}Sb_{0.09}$ can be carried out in future to see what effect the higher temperatures have on this material's elastic properties. The effects of elastically harder or elastically softer materials on the elastic properties of this ternary semiconductor alloy can also be studied by synthesising bi-layers of this alloy with such materials. Depending on the ultimate application of both materials studied in this work, high pressure SBS studies cannot be ruled out as a possible research interest.

References

Chapter 1

[1.1] Stoddart, P.R. (1999). *Surface Brillouin Scattering Studies of High-Temperature Elasticity*, PhD thesis, University of the Witwatersrand, Johannesburg.

[1.2] Sandercock, J.R. (1982). Trends in Brillouin scattering: Studies of Opaque materials, Supported Films and Central Modes, in *Light Scattering in Solids III: Recent Results*. Topics in Applied Physics, Vol 51, edited by Cardona, M. and Guntherdt, G. (Springer, Berlin), pp 173-206.

[1.3] Stoddart, P.R., Comins, J.D. and Every, A.G. (1995). *Phys. Rev.* **B51**, 17574.

[1.4] Crowhurst, J.C., Hearne, G.R., Comins, J.D., Every, A.G. and Stoddart, P.R. (1999). *Phys. Rev.* **B60**, R14 990.

[1.5] Comins, J.D., Every, A.G., Stoddart, P.R., Zhang, X. and Crowhurst, J.C. and Hearne, G.R. (2000). *Ultrasonics*, **38**, 450.

[1.6] Every, A.G., Pang, W., Comins, J.D. and Stoddart, P.R., (1998). *Ultrasonics*, **36**, 223.

[1.7] Comins, J.D. (2001). Chapter 15, in *Handbook of Elastic Properties of Solids, Liquids and Gases. Volume I: Dynamic Methods for Measuring the Elastic Properties of Solids*, edited by Levy, Bass and Stern (Academic Press).

[1.8] Nye, J.F. (1969). *Physical Properties of Crystals* (Oxford University Press, Oxford).

[1.9] Every, A.G. (2001). Chapter 1, in *Handbook of Elastic Properties of Solids, Liquids and Gases. Volume I: Dynamic Methods for Measuring the Elastic Properties of Solids*, edited by Levy, Bass and Stern (Academic Press).

[1.10] Royer, D. and Dieulesaint, E.M. (1984). *J. Acoust. Soc. Am.* **76**, 1438.

[1.11] Marvin, A.M., Bortolani, V., Nizzoli, F. and Santoro, G. (1980). *J. Phys* **C13**, 1607.

[1.12] www.soest.hawaii.edu/~zinin/Zi-Brillouin.html. Retrieved December 2009.

[1.13] Nizzoli, F. and Sandercock, J.R. (1990). In *Dynamical Properties of Solids, vol. 6: The Modern Physics of Phonons: Transport, Surfaces and Simulations*, p. 281, edited by Horton, G.K. and Maradudin, A.A. (Amsterdam, North Holland).

[1.14] Mills, D.L. and Subbaswamy, K.R. (1981). *In Progress in Optics*, p.45, vol. 19, Wolf, E., ed., Amsterdam, New Holland.

[1.15] Loudon, R. (1978). *Phys. Rev. Lett*. **40**, 581.

[1.16] Loudon, R. (1978). J. *Phys.* **C11**, 403.

[1.17] Subbaswamy, K.R. and Maradudin, A.A. (1978). *Phys. Rev*. **B18**, 4181.

[1.18] Velasco, V.R. and Garcia-Moliner, F. (1980). *J. Phys*. **C13**, 2237.

[1.19] Every, A.G., Kim, K.Y. and Mazenev, A.A., (1997). *J. Acoust. Soc. Am*. **102**, 1346.

[1.20] Zhang, X., Comins, J.D., Every, A.G., Stoddart, P.R., Pang, W. and Derry, T.E. (1998). *Phys. Rev*. **B58**, 13677.

[1.21] Loudon, R. and Sandercock, J.R. (1980). *J. Phys.* **C13**, 2609.

[1.22] Maradudin, A.A. and Mills, D.L. (1975). *Phys. Rev*. **B11**, 1392.

[1.23] Agarwal, G.S. (1977). *Phys. Rev*. **B15**, 2371.

[1.24] Marvin, A.M., Toigo, F. and Celli, V. (1975). *Phys. Rev*. **B11**, 2777.

[1.25] Ngoepe, P.E. (1989). *High Temperature Studies of Fast-ion Conductors using Brillouin Scattering Techniques*, PhD thesis, University of the Witwatersrand, Johannesburg.

[1.26] Crowhurst, J.C. (2001). *Surface Brillouin scattering studies of high-pressure elasticity and nickel-vanadium multilayers*, PhD thesis, University of the Witwatersrand, Johannesburg.

Chapter 2

[2.1] Sandercock, J.R. (1982). Trends in Brillouin scattering: Studies of Opaque materials, Supported Films and Central Modes, in *Light Scattering in Solids III: Recent Results*. Topics in Applied Physics, Vol 51, edited by Cardona, M. and Guntherdt, G. (Springer, Berlin), pp 173-206.

[2.2] Operation manual of Spectra-Physics Model 171 argon ion laser.

[2.3] Sandercock, J.R. (1971). The design and use of a stabilised multipassed interferometer of high contrast ratio, in *Proceedings of the second International Conference on Light Scattering in Solids, Paris*, edited by Balkanski, M. (Flammarion, Paris), pp 9 – 12.

[2.4] Mock, R., Hillebrands, B. and Sandercock, J.R. (1987). *J. Phys. Instr*. **20**, 656.

[2.5] EG&G Optoelectronics Canada (1997) *Model SPCM-200-PQ instruction manual*.

[2.6] Sandercock, J.R. (1993). *Operator Manual for tandem interferometer*, ver. 3.

[2.7] Sussner, H. and Vacher, R. (1979). *Appl. Opt.* **18**, 3815.

Chapter 3

[3.1] www.memsnet.org. Retrieved January 2004.

[3.2] Saleh, R and Nickel, N.H. (2003). *Thin Solid Films*, **427**, 226.

[3.3] Sharpe Jr, W.N., Yuan, B., Vaidyanathan, R. and Edwards, R.L. (1997) *Proceedings of the 10th IEE International workshop on Microelectromechanical Systems*, Nagoya, Japan, pp 424-429.

[3.4] Mathe, B.M. (2007). *Surface Brillouin scattering studies of elastic properties of materials at high temperatures*, PhD thesis, University of the Witwatersrand, Johannesburg.

[3.5] Eguiliz, A.G. and Maradudin, A.A. (1983). *Phys. Rev*. **B28**, 728.

[3.6] Horn, F. H. (1955). *Phys. Rev.* **97**, 1521.

[3.7] Greek, S.,Ericson, F., Johansson, S., Furtsch, M. and Rump, A. (1999). *J. Micromech. Microeng.* **9**, 245.

[3.8] Anastassakis, E. and Liarokapis, E. (1987). *J. Appl. Phys*. **62**(8), 3346.

Chapter 4

[4.1] Fukui, T. and Horikoshi, Y. (1980). *Jpn. J. Appl. Phys*. **19**, L53.

[4.2] Lee, G.S., Lo, Y., Lin, F., Bedair, S.M. and Laidig, W.D. (1985). *Appl. Phys. Lett*. **47**, 1219.

[4.3] Giani, A., Podlecki, J., Pascal-Delannoy, F., Bougnot, G., Gouskov, L. and Catinaud, C. (1995). *J. Cryst. Growth*, **148**, 25.

[4.4] Sze, S.M. (1981). *Physics of Semiconductor Devices*. (John Wiley, New York).

[4.5] Zotova, N.V., Kizhaev, S.S., Molchanov, S.S., Popova, T.B. and Yakovlev, Yu.P. (2000). *Semiconductors*, **34**(12), 1402.

[4.6] Biefeld, R.M. (1986). *J. Cryst. Growth*, **75**, 255.

Publications

1. Tlali, S.B., Mathe, B.A., Kotane, L.M., Schöning, F.R.L, Comins, J.D., Every, A.G., Sithole, H.M., Ngoepe, P.E. and Wright, K.V. (2004). *Brillouin scattering studies and computational simulations of the elastic properties of pyrite (FeS_2) at high temperatures*. *Phys. Stat. Sol.* (c) **1**, No. 11, 3073.

2. Kotane, L.M., Comins, J.D., Every, A.G. and Botha, J.R, *Measurement of the elastic constants of single crystal $InAs_{0.91}Sb_{0.09}$ by surface Brillouin scattering.* Paper in preparation.

Conference presentations

1. Tlali, S.B., Mathe, B.A., Kotane, L.M., Schöning, F.R.L, Comins, J.D., Every, A.G., Sithole, H.M., Ngoepe, P.E. and Wright, K.V., *Brillouin scattering studies of iron pyrite (FeS_2) at high temperature*, 48th Annual Conference of the SAIP, in Stellenbosch, South Africa (2003).

2. Kotane, L.M., Mathe, B.A., Comins, J.D. and Every, A.G., *High temperature surface Brillouin scattering study of boron-doped silicon (B-Si)*, 49th Annual Conference of the SAIP, in Bloemfontein, South Africa (2004).

3. Kotane, L.M., Comins, J.D., Every, A.G. and Botha, J.R., *Surface Brillouin scattering measurement of the elastic constants of single crystal $InAs_{0.91}Sb_{0.09}$*, Laser Ultrasonics symposium, in Bordeaux, France (July 5 – 8, 2010). Abstract submitted for presentation.